Pergamon

Geochimica et Cosmochimica Acta, Vol. 66, No. 3, pp. 521–540, 2002

0016-7037/02 $22.00 + .00

PII S0016-7037(01)00782-7

Elemental and isotopic fractionation of Type B calcium-, aluminum-rich inclusions: Experiments, theoretical considerations, and constraints on their thermal evolution

FRANK M. RICHTER,[1,*] ANDREW M. DAVIS,[1,2] DENTON S. EBEL,[1] and AKIHIKO HASHIMOTO[3]

[1]Department of the Geophysical Sciences, University of Chicago, 5734 South Ellis Avenue, Chicago, IL 60637, USA
[2]Enrico Fermi Institute, University of Chicago, 5640 South Ellis Avenue, Chicago, IL 60637, USA
[3]Graduate School of Earth and Planetary Sciences, Hokkaido University, Sapporo, Japan

(*Received February* 1, 2001; *accepted in revised form July* 30, 2001)

Abstract—Experiments exposing Type B calcium-, aluminum-rich inclusion (CAI)-like melts at high temperatures to high vacuum or reducing hydrogen-rich gas mixtures were used to determine the rates and consequences of elemental and isotopic fractionation by evaporation. Silicon and magnesium were found to evaporate much faster than calcium and aluminum, and the resulting residual liquid trajectories in composition space are reproduced via a thermodynamic model for the saturation vapor pressure of the evaporating species. Isotopic fractionations associated with evaporation were measured for magnesium. The resulting relationship between fraction of magnesium lost and enrichment of the residue in the heavy isotopes of magnesium follows a Rayleigh fractionation curve with a fractionation factor that is close to, but not exactly, the theoretically expected value. The rate of evaporation is found to be a strong function of temperature, oxygen fugacity, and melt composition, which can be understood and modeled in terms of the dependence of the saturation vapor pressures on these variables. The relationship between evaporation rate, which we measure, and calculated saturation vapor involves empirical evaporation coefficients that we find to be significantly less than one ($\sim$0.1). Analytical and numerical models are used to characterize how diffusion in both the melt and in the surrounding gas affects evaporation rates and the degree of chemical and isotopic fractionation. The experimental data and theoretical considerations are combined to give a parameterization of the rates and consequences of evaporation of Type B CAI-like liquids, which is then used to translate the measured isotopic fractionation of Type B CAIs into constraints on their thermal history. Cooling rates of the order of 10°C per hour are indicated.

1. INTRODUCTION

Our understanding of the earliest history of the solar system comes from a variety of sources, including astronomical observations of protoplanetary disks around young stars, numerical simulations of particular stages and processes in the evolution of such disks, and chemical and textural analyses of solar system materials. Boss (1998) reviewed these lines of evidence and inference in the specific context of temperatures in protoplanetary disks. Our focus here will be on certain aspects of the cosmochemical evidence as it relates to thermal evolution. We present new laboratory data on the rate and consequences of high-temperature evaporation of particular solar system materials (calcium- and aluminum-rich refractory inclusions) and use these to develop constraints regarding their thermal histories.

Calcium-, aluminum-rich inclusions (CAIs) in Allende and other CV3 chondrites have been studied in considerable detail because they are among the most primitive objects formed in the solar system. CAIs are regarded as primitive for the following reasons: (1) they yield the oldest U-Pb dates of any solar system objects (Allègre et al., 1995); (2) they have the highest amounts of daughter products of short-lived isotopes of any solar system object (e.g., MacPherson et al., 1995); and (3) they contain the same minerals as those predicted to be in equilibrium with a gas of solar composition at high temperature (e.g., Grossman, 1972, and further discussion below regarding bulk composition). The most detailed studies involve the Type B CAIs. These are large (typically 1 cm in diameter), coarse-grained inclusions with easily identifiable crystals of spinel, melilite, fassaite, and anorthite. However, when the published chemical compositions of Type B (and also Type A) inclusions are considered in detail, they do not correspond to the predicted compositions derived from thermodynamic calculations of condensation from a solar gas.

Grossman et al. (2000) considered two reasons for this difference. The first involves uncertainties in the reported bulk composition of refractory inclusions due to possible over- or underestimation of the amount of spinel. The fact that many published compositions of Type A and B refractory inclusions are not chondritic in calcium-to-aluminum ratio, despite the difficulty in fractionating calcium from aluminum after magnesium and silicon begin to condense, was taken as an indication that the published compositions are likely to be in error. However, even after the published compositions are adjusted to solar Ca/Al by the addition or subtraction of appropriate amounts of spinel, they still fail to lie along the calculated condensation trajectories. In almost every case, the corrected compositions of the Type B inclusions are significantly lower in MgO, and possibly lower in SiO_2 as well, than calculated condensates. Thus, if the precursors of the Type B inclusions did in fact originally condense from a solar gas, their compositions must have been modified at some later stage by the preferential loss of magnesium, and quite possibly silicon, relative to calcium and aluminum. The most likely mechanism

* Author to whom correspondence should be addressed (richter@geosci.uchicago.edu).

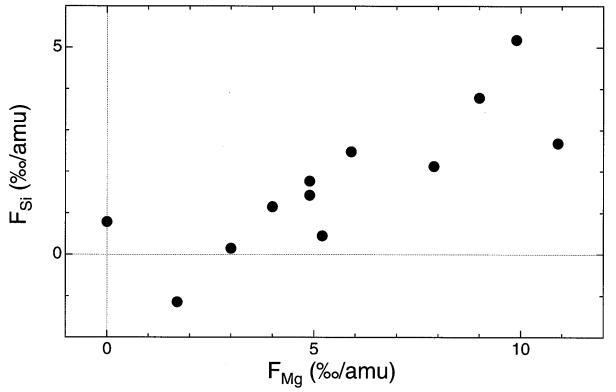

Fig. 1. Silicon and magnesium isotopic composition of normal (i.e., free of large nucleosynthetic isotopic anomalies) Type B CAIs (‰ amu^{-1}) relative to the terrestrial value from the compilation by Clayton et al. (1988). The general pattern of correlated enrichment in the heavy isotopes of silicon and magnesium is also found in residues of molten silicates partially evaporated in high-temperature vacuum furnaces (Davis et al., 1990; Wang et al., 2001), supporting the view that the Type B CAIs are themselves evaporation residues.

for this is evaporation during a reheating event, which would fractionate the elements because magnesium and silicon are significantly more volatile than calcium and aluminum. Several independent lines of evidence suggest that evaporation did in fact affect the composition of Type B CAIs. To begin with, textural evidence suggests the Type B CAIs were once partially molten, which requires reheating to at least several hundred degrees Celsius above their condensation temperature ($T > 1400$°C; Stolper, 1982; Stolper and Paque, 1986). If this reheating took place in an environment undersaturated by prior condensation, then the inclusions would preferentially lose magnesium and silicon relative to the much less volatile calcium and aluminum. The second, even more compelling, evidence for evaporation comes from the silicon and magnesium isotopic compositions of Type A and Type B CAIs. They are often found to be mass-fractionated by several ‰ amu^{-1} (per mil. per atomic mass unit) in favor of the heavy isotopes of silicon and magnesium (Clayton et al., 1988, and Fig. 1). Laboratory experiments have shown that evaporative loss of silicon and magnesium from a melt will produce residues that are similarly enriched in the heavy isotopes of silicon and magnesium (Davis et al., 1990). Grossman et al. (2000) went on to point out that the elemental and isotopic data from Type A and B CAIs are remarkably consistent with each other, in the sense that the range of departures of corrected CAI compositions from the condensation curve (presumed to represent the amount of lost silicon and magnesium) are the same as the range of silicon and magnesium that would have to have been removed by evaporation to produce the range of measured isotopic fractionations.

The present study has as its point of departure the view that the correlated variations in silicon and magnesium isotopic composition of Type B CAIs (Fig. 1) are the result of evaporative losses of silicon and magnesium during a high-temperature, partially molten stage. The main goal of the work is to provide a representation of the evaporative effects as function of temperature, pressure, and composition. We accomplish this by laboratory experiments run under a variety of conditions to calibrate a thermodynamics-based model of the evaporation process. The model, together with the measured magnesium isotopic composition of Type B CAIs, is then used to argue that the typical Type B CAI cooled from a partially molten state at a rate of ~10°C h^{-1}.

2. PREVIOUS EXPERIMENTS RELATING TO THE IGNEOUS PETROLOGY AND THERMAL HISTORY OF TYPE B CAIS

The main reason we focused this study on materials with Type B CAI-like compositions (~29 wt% CaO, 29% Al_2O_3, 31% SiO_2, 10% MgO, and 1% TiO_2; Stolper, 1982) is that the Type Bs are by far the best studied of all the "igneous" CAIs. The typical Type B CAI is spheroidal and about a centimeter in diameter. The major minerals are spinel ($MgAl_2O_4$), melilite (a solid solution of gehlenite, $Ca_2Al_2SiO_7$, and åkermanite, $Ca_2MgSi_2O_7$), an aluminum-, titanium-rich clinopyroxene (fassaite) and anorthite ($CaAl_2Si_2O_8$). Type B CAIs are subdivided into B2s, which have a relatively uniform distribution of the major mineral phases, and B1s, which have a melilite-dominated outer mantle surrounding a spinel + melilite + anorthite + fassaite core. Laboratory experiments on synthetic Type B compositions have established the following attributes.

(1) The liquidus temperatures are of the order of 1550°C, and the equilibrium crystallization sequence is spinel, followed by melilite at ~1400°C, anorthite at ~1260°C, and finally fassaite at ~1230°C (Stolper, 1982).

(2) The melilite is zoned with the first melilite to crystallize having $Åk_{\sim 20}$, increasing to $Åk_{\sim 45}$ when plagioclase begins to crystallize (Stolper, 1982), and reaching $Åk_{65-70}$ at the end of melilite crystallization.

(3) Experiments in which synthetic Type B compositions are first partially melted and then cooled at a controlled rate show that the resulting mineral textures are sensitive to both the peak temperature and subsequent cooling rate. Euhedral melilite crystals similar to those found in Type B CAIs are best reproduced by peak temperatures of ~1400°C (partially molten with ~5% spinel) and cooling rates slower than 50°C h^{-1} (Stolper and Paque, 1986). Cooling rates faster than 50°C h^{-1} produce distinctively blocky or dendritic melilite textures that are not seen in Type B CAIs.

(4) Melilite crystals in Type B inclusions often show a reversal in Åk zoning such that there is a brief decline in the Åk values of late-crystallizing melilite. MacPherson et al. (1984) interpreted this reversal as being due to fassaite crystallizing before anorthite, which is not the equilibrium order but is nevertheless found to occur in laboratory experiments with cooling rates as low as 0.5°C h^{-1}. This should be regarded as an upper bound on the slowest allowable cooling rate given that even slower cooling rates might also produce reversed zoning.

(5) More than half of the titanium in fassaite crystals in Type B CAIs can be Ti^{+3} (Dowty and Clark, 1973). Beckett (1986) measured Ti^{+3}/Ti^{+4} ratios in fassaite from experiments in which Type B CAI-like compositions were cooled and crystallized at a variety of oxygen fugacities (f_{O_2}). He found that high Ti^{+3}/Ti^{+4} ratios are only produced at low f_{O_2} and inferred that CAIs crystallized in a very reducing environment with more or less solar f_{O_2}.

(6) Type B CAI compositions heated to T $\geq$ 1400°C in vacuum or in 2×10^{-4} bar of hydrogen lose silicon and magnesium (relative to calcium and aluminum) by evaporation. The residues from these experiments are enriched in the heavy isotopes of magnesium (Richter et al., 1999a; Parsad et al., 2000), and though not measured, presumably similarly enriched in the heavy isotopes of silicon as well.

Grossman et al. (2000) combined the above experimental results with condensation calculations to give the following account of the origin and evolution of the Type B CAIs. The precursor materials of the Type B CAIs condensed as solids from a solar composition gas at temperatures in the range 1000°C ($P = 10^{-6}$ bar) − 1200°C ($P = 10^{-3}$ bar). They were later partially melted by reheating to ~1400°C and then cooled at rates between 50 and 0.5°C h^{-1}. During reheating, the CAIs lost up to 50% of their original magnesium and up to 25% of their silicon by evaporation. The associated preferential evaporation of the lighter isotopes resulted in the CAIs becoming enriched in the heavy isotopes of silicon and magnesium as shown in Figure 1. Because in what follows we will place special emphasis on the rates of evaporation, it is important to keep in mind that the Ti^{+3}/Ti^{+4} ratio of the CAIs is regarded as evidence of their having crystallized in a very reducing environment (Beckett, 1986). Thus it is likely that hydrogen was the dominant gas during the reheating episode; and hydrogen, as we will see below, has a major effect on the evaporation kinetics.

3. ARGUMENTS BASED ON TRACE ELEMENT PARTITIONING

Davis and MacPherson (1996) argued on the basis of trace element evidence that the cooling rates of Type B CAIs were most likely to have been at the higher end of the 0.5 to 50°C h^{-1} range noted above. Their argument was based on the observation that incompatible trace element concentrations in melilite from Type B CAIs are in some cases (most notably barium) significantly higher than what one would expect given the existing experimental data on melilite/melt partitioning by Beckett et al. (1990). In the case of barium, the concentration in melilite is not much different than that in the inclusion as a whole, whereas the barium melilite/melt distribution coefficient had been measured by Beckett et al. (1990) to be ~0.04 in dynamic crystallization experiments with cooling rates of 2°C h^{-1}. Davis and MacPherson (1996) suggested that the reason natural melilite had incorporated such surprisingly large amounts of incompatible trace elements was the development of incompatible-element–rich diffusive boundary layers in the melt adjacent to rapidly growing melilite crystals. For sufficiently rapid crystal growth relative to diffusion in the surrounding melt, the concentration in the crystal will approach that of the melt reservoir regardless of the partition coefficient. They concluded that because such enriched boundary layers had not affected partitioning in the Beckett et al. (1990) dynamic crystallization experiments, natural CAIs must have cooled at rates significantly faster than the 2°C h^{-1} of those experiments.

Davis et al. (1996) and Simon et al. (1996) reported the results of a set of laboratory experiments designed to test the Davis and MacPherson (1996) suggestion. Dynamic crystallization experiments similar to those of Beckett et al. (1990) were carried out with cooling rates of 2°C h^{-1}, 20°C h^{-1}, and 75°C h^{-1}. As had been found earlier by Stolper and Paque (1986), the melilite crystallized at 75°C h^{-1} is distinctly blocky and thus this cooling rate is believed to be somewhat faster than that of the Type B CAIs. Ion microprobe analyses of the melilite and surrounding quenched glass from all three cooling rates yielded distribution coefficients in good agreement with those reported by Beckett et al. (1990) and thus no significant effect of cooling rate on the partitioning behavior. It follows that the trace element data do not provide a constraint on the cooling rate, at least not for the reasons suggested by Davis and MacPherson (1996).

4. THEORETICAL CONSIDERATIONS

The laboratory evaporation experiments reported in this article were designed to test and complement a generally accepted theoretical description of evaporation kinetics when applied to Type B CAI-like liquids. The evaporative flux from a solid or molten surface into a surrounding gas is given by the Hertz-Knudsen equation (see Hirth and Pound, 1963),

$$J_i = \sum_{j=1}^{n} \frac{\gamma_{ij} P_{ij,sat}}{\sqrt{2\pi m_{ij} RT}}, \quad (1)$$

where J_i is the flux of element or isotope i (moles per unit area per unit time), γ_{ij} is the evaporation coefficient for the *j*th gas species containing i, $P_{ij,sat}$ is the saturation vapor pressure of j, m_{ij} is the molecular weight of j, R is the gas constant, and T is the absolute temperature. The summation is over all gas species j containing i. Laboratory evaporation experiments are needed in connection with the evaporation coefficients. Eqn. 1 gives a quantitative measure of evaporation rates only after the γ_{ij} values have been determined for the system of interest by combining laboratory data for J_i with a thermodynamic model for the speciation and saturation vapor pressures.

J_i in Eqn. 1 represents the flux from the surface whether or not recondensation is taking place. The net evaporation rate ($J_{i,net}$) measured in a laboratory experiment is the difference between evaporation and recondensation, which can be written as

$$J_{i,net} = \sum_{j=1}^{n} \frac{\gamma_{ij}(P_{ij,sat} - P_{ij})}{\sqrt{2\pi m_{ij} RT}}, \quad (2)$$

where P_{ij} is the pressure at the evaporating surface of the *j*th gas species containing the element or isotope i. Eqn. 2 assumes that condensation coefficients are the same as the evaporation coefficients, which must be true at least in the limit $P_{ij} \rightarrow P_{ij,sat}$. In the simple but often applicable case when a single gas species dominates the budget of the element of interest (i.e., n = 1), Eqns. 1 and 2 can be combined to give

$$J_{i,net} = J_i\left(1 - \frac{P_i}{P_{sat}}\right), \quad (3)$$

showing that only evaporation experiments run at sufficiently low pressure (i.e., $P_i/P_{i,sat} \ll 1$) will directly determine the free evaporation rate J_i.

Assuming again that the equilibrium speciation in the gas is dominated by a single species i and furthermore that $P_i/P_{i,sat} \ll 1$ (i.e., no significant recondensation), the relative rate of loss by evaporation of two isotopes of i (denoted by subscripts i,1 and i,2) will be given by

$$\frac{J_{i,2}}{J_{i,1}} = \frac{P_{i,2,sat}}{P_{i,1,sat}} \sqrt{\frac{m_{i,1}}{m_{i,2}}} \tag{4a}$$

$$= R_{2,1} \sqrt{\frac{m_{i,1}}{m_{i,2}}}, \tag{4b}$$

where $R_{2,1}$ is the atom ratio of isotope 2 to isotope 1 at the evaporating surface. In writing Eqn. 4b, we assumed that isotopes mix ideally and that at the high temperatures of interest we can ignore any equilibrium isotope fractionation between the condensed phase and the gas. With these assumptions, the ratio of the saturation vapor pressures equals the atom ratio in the condensed phase. If we add the further restriction that the evaporating material remain effectively uniform in composition despite the selective chemical losses from its surface (i.e., that diffusion or convection maintain homogeneity at all times), then the isotopic composition of the residue will evolve by Rayleigh fractionation as given by

$$R_{2,1}^{res} = R_{2,1}^{0} F^{(\alpha - 1)}, \tag{5}$$

where $R_{2,1}^{0}$ is the initial isotopic composition of the evaporating material, F is the fraction of isotope 1 remaining in the residue, and $\alpha = \sqrt{m_{i,1}/m_{i,2}}$.

Rayleigh fractionation as given by Eqn. 5 requires $P_i/P_{i,sat} \ll 1$ and that transport within the residual evaporating material be sufficiently fast to maintain chemical and isotopic homogeneity. Neither of these conditions need to have prevailed during the evaporation of the Type B CAIs. Departures from perfect Rayleigh fractionation due to a surrounding finite pressure of the evaporating species have been discussed by Tsuchiyama et al. (1999) for evaporation into a closed system and by Humayun and Cassen (2000) for evaporation into a gas of fixed $P_{i,gas}/P_{i,sat}$ and fixed isotopic composition. We consider the case of evaporation into a surrounding gas (mostly hydrogen in our applications) in which the pressure of the evaporating species is specified only far from the evaporating surface. The mathematical representation of the molar density $C_i(r,t)$ of an evaporating species (proportional to pressure in an ideal and isothermal gas) outside a spherical source of radius a is

$$\frac{\partial C_i}{\partial t} = D_i \left(\frac{\partial^2 C_i}{\partial r^2} + \frac{2}{r} \frac{\partial C_i}{\partial r} \right), \tag{6}$$

with initial conditions $C_i(r,0) = C_{i,0}$ for $r > a$ and boundary conditions

$$C_i(\infty, t) = C_{i,0} \text{ at } r = \infty \tag{6a}$$

and

$$D_i \frac{\partial C_i}{\partial r} = -J_{i,net} \text{ at } r = a. \tag{6b}$$

D_i is the interdiffusion coefficient of i in the surrounding gas and $J_{i,net}$ is the net flux of i per unit area from the evaporating surface. We are specifically interested in recondensation at the surface, and therefore focus on $C_i(a,t)$, the solution to Eqn. 6 evaluated at $r = a$. The desired solution, in terms of the similarity variable $\xi = D_i t/a^2$, is given by

$$C_i(a, t) = C_{i,0} + \frac{a J_{i,net}}{D_i} (1 - e^{\xi} \text{erfc} \sqrt{\xi}) \tag{7}$$

The explicitly time-dependent quantity $e^{\xi}\text{erfc}\sqrt{\xi}$ tends to zero as ξ becomes large (e.g., $e^{\xi}\text{erfc}\sqrt{\xi} < 0.02$ for $\xi = 1000$), thus for most purposes the asymptotic solution $C_i(a,t) = C_{i,0} + aJ_{i,net}/D_i$ is all that is required. The asymptotic form can be used for all times $t > 1000\ a^2/D_i$ (~1 s for a = 1 cm and typical values of D_i for diffusion of gaseous species through hydrogen at T = 1400°C and $P_{H_2} = 10^{-2}$ bar) whenever all other properties of the system (e.g., $J_{i,net}$ or T) do not change significantly on this time scale. For our present purposes, the asymptotic form of Eqn. 7 is perfectly adequate.

We now rewrite Eqn. 2 for n = 1 by using $P_i = P_{i,\infty} + (aJ_{i,net}/D_i)RT$, where $P_{i,\infty} = C_{i,0}RT$ is the far-field ($r \to \infty$) pressure of species i. Thus,

$$J_{i,net} = \frac{\gamma_i (P_{i,sat} - P_i)}{\sqrt{2\pi m_i RT}} = \frac{\gamma_i (P_{i,sat} - P_{i,\infty})}{\sqrt{2\pi m_i RT}} - \frac{\gamma_i J_{i,net} \frac{a}{D_i} RT}{\sqrt{2\pi m_i RT}} \tag{8}$$

which, when solved for $J_{i,net}$, gives

$$J_{i,net} = \frac{J_i \left(1 - \frac{P_{i,\infty}}{P_{i,sat}}\right)}{1 + \frac{\gamma_i a}{D_i} \sqrt{\frac{RT}{2\pi m_i}}}. \tag{9}$$

J_i in Eqn. 9 is the free (vacuum) evaporation rate as defined by Eqn. 1 when n = 1. We can now see that free evaporation ($J_{i,net} = J_i$) will only be realized when the far-field pressure is low ($P_{i,\infty} \ll P_{i,sat}$) and diffusion in the surrounding gas is sufficiently fast (D_i sufficiently large) for the denominator of Eqn. 9 to be effectively equal to one.

We now consider the factors controlling chemical and isotopic gradients within the evaporating material itself. Eqn. 9 provides the surface flux that is used in the (r = a) boundary conditions for the conservation equations for the evolution of the elemental and isotopic composition of both the evaporating material (Eqn. 10 below) and in the surrounding gas (Eqn. 6). A simplified (monomineralic) version of the conservation equation in a sphere of radius a is

$$\frac{\partial C_{i,m}}{\partial t} = D_{i,m} \left(\frac{\partial^2 C_{i,m}}{\partial r^2} + \frac{2}{r} \frac{\partial C_{i,m}}{\partial r} \right) + \frac{1}{\phi} \frac{\partial \phi}{\partial t} (C_{i,xtl} - C_{i,m}), \tag{10}$$

with

$$D_{i,m} \frac{\partial C_{i,m}}{\partial r} = -J_{i,net} - C_{i,m} \frac{\partial a}{\partial t} \text{ at } r = a(t), \tag{10a}$$

$$\frac{\partial C_{i,m}}{\partial r} = 0 \text{ at } r = 0, \tag{10b}$$

and

$$\frac{\partial a}{\partial t} = -\sum J_{j,net} v_j. \tag{10c}$$

Table 1. Run conditions, sample sizes, chemical compositions, isotopic compositions, and derived parameters from CAI evaporation experiments.[a]

Sample	Pressure (bar)	T (°C)	Avg. area (cm^2)	MgO (wt%)	SiO_2 (wt%)	CaO (wt%)	Al_2O_3 (wt%)	run time (min)	J_{Mg} (mol cm^{-2} s^{-1})	J_{Si} (mol cm^{-2} s^{-1})	γ_{Mg}	γ_{Si}	% Mg loss	F_{Mg} (‰ amu^{-1})
B-133-0				11.94	46.04	22.64	19.30	0					≡0.00	≡0.00
B-133-11	$<10^{-9}$	1800	0.12	3.30	25.90	38.18	32.55	60	9.14×10^{-8}	1.88×10^{-7}	0.21	0.20	83.62	20.13 ± 0.87
B-133-12	$<10^{-9}$	1800	0.14	9.55	32.25	31.55	26.69	60	6.78×10^{-8}	2.03×10^{-7}	0.17	0.17		
B-133-13	$<10^{-9}$	1800	0.15	1.88	23.65	40.10	34.37	60	7.73×10^{-8}	1.56×10^{-7}	0.18	0.18		
B-133-15	$<10^{-9}$	1800	0.19	1.06	22.75	41.31	34.88	90	8.28×10^{-8}	1.64×10^{-7}	0.21	0.20		
B-133-16	$<10^{-9}$	1800	0.13	0.53	22.07	41.67	35.65	90	8.65×10^{-8}	1.66×10^{-7}	0.22	0.20	97.59	45.73 ± 2.16
B-133-17	$<10^{-9}$	1800	0.19	11.97	36.94	27.62	23.44	30	3.71×10^{-8}	1.82×10^{-7}	0.12	0.13	17.63	1.33 ± 1.81
B-133-19	$<10^{-9}$	1800	0.26	12.26	42.50	24.43	20.75	15	2.84×10^{-8}	1.97×10^{-7}	0.10	0.11	4.66	0.29 ± 1.38
B-113-0				12.67	47.89	19.66	19.78						≡0.00	≡0.00
B-113-3	1	1400		11.33	40.84	25.29	22.54	150					23.82	−0.40 ± 0.48
B-113-4	1	1400		7.03	36.28	30.05	26.63	300					60.10	0.26 ± 0.57
B-113-8	$<10^{-9}$	1800	0.161	11.63	34.72	26.92	26.73	30	5.74×10^{-8}	2.06×10^{-7}	0.15	0.14	32.53	2.53 ± 1.70
B-113-9	$<10^{-9}$	1800	0.135	6.60	29.30	32.15	32.00	60	9.24×10^{-8}	2.14×10^{-7}	0.24	0.15	53.46	6.75 ± 1.89
B-113-10	$<10^{-9}$	1700	0.131	8.77	32.54	29.47	29.22	180	1.66×10^{-8}	4.24×10^{-8}	0.18	0.14	67.80	12.43 ± 2.09
BCAI-0				17.84	37.04	24.61	20.51						≡0.00	≡0.00
BCAI-ss1	1.87×10^{-4}	1500	0.0672	15.00	35.97	27.75	21.29	30	4.12×10^{-8}	2.70×10^{-8}	0.051	0.058	19.00	4.78 ± 0.76
BCAI-ss2	1.87×10^{-4}	1500	0.0621	6.11	30.60	33.27	30.04	120	3.68×10^{-8}	2.73×10^{-8}	0.047	0.068	76.61	19.55 ± 1.33
BCAI-s1	1.87×10^{-4}	1500	0.168	10.84	34.24	30.13	24.79	120	3.12×10^{-8}	2.10×10^{-8}	0.039	0.048	49.71	8.62 ± 1.86
BCAI-s3	1.87×10^{-4}	1500	0.134	2.72	28.15	35.83	33.30	240	3.51×10^{-8}	2.67×10^{-8}	0.048	0.069	90.59	30.72 ± 1.48
BCAI-m1	1.87×10^{-4}	1500	0.407	16.93	35.97	26.22	20.88	60	2.10×10^{-8}	2.30×10^{-8}	0.026	0.049	6.78	2.11 ± 0.78
BCAI-m2	1.87×10^{-4}	1500	0.425	13.43	33.18	26.89	26.50	180	2.34×10^{-8}	2.13×10^{-8}	0.029	0.050	41.70	7.40 ± 1.16

[a] J_{Mg} and J_{Si} are the evaporation rates of magnesium and silicon, respectively. γ_{Mg} and γ_{Si} are the corresponding evaporation coefficients. F_{Mg} is the magnesium isotopic composition of the residue in per mil per atomic mass unit relative to the starting material.

$C_{i,m}$ and $C_{i,xtl}$ are respectively the molar density of the element or isotope i in the melt and in a mineral in equilibrium with the melt, ϕ is the melt fraction, and $D_{i,m}$ is the effective diffusion coefficient of i in the melt. v_j is the molar volume of species j and the summation is taken overall evaporating species. The last term on the right-hand side of Eqn. 10 represents an effective source or sink of i due to changes in the melt fraction ϕ. Specifying the local value of $(1/\phi)\partial\phi/\partial t$ as the temperature and composition of the system evolve requires additional information in the form of a thermodynamic model for the system.

The equations given above (specifically Eqns. 1, 6, 9, and 10), together with thermodynamic models for the various phases, provide a complete specification of evaporation, subject to certain simplifications regarding the number of gas species and minerals considered. Consideration of multiple gas species and multiple minerals is, in principle, straightforward, but cumbersome in terms of notation. Because we know of no theoretical approach for calculating the evaporation coefficients for the systems of interest here, a major focus of the experiments discussed in the following sections is to measure evaporation rates from molten Type B CAI-like compositions and use these to calculate evaporation coefficients as a function of temperature, gas pressure, and composition. The experiments will also test certain aspects of the theoretical and thermodynamic description of the system when we compare the predicted and measured elemental and isotopic evolution of the evaporative residues.

5. EXPERIMENTAL AND ANALYTICAL METHODS

5.1. Starting Materials

The starting materials used in the evaporation experiments (Table 1) were synthesized in 1-g batches by first mixing pure oxides of silicon, aluminum, and magnesium with $CaCO_3$ in proportions that, when decarbonated, give the desired composition. The mixtures were heated slowly in air to 1500°C, held at this temperature for ~24 h, and then rapidly quenched. The resulting glass was ground to a fine powder, and aliquots of this powder were used to make the experimental samples by placing varying amounts (5 to 70 mg) onto preweighed platinum or iridium wire loops. Each sample was then put into a gas-mixing furnace and heated to 1400°C for several hours in a H_2/CO_2 mixture with an f_{O_2} corresponding to iron-wüstite ($\log f_{O_2} = -9.8$). This produced a hardened sample that could be weighed and measured for surface area without loss of sample material. We confirmed that samples held at 1400°C for several hours in a gas mixture with $\log f_{O_2} \approx -10$ suffer no measurable evaporative weight loss of sample or wire loop. Platinum metal and molten silicates can suffer significant evaporative weight loss if heated in a more reducing environment while iridium will evaporate under more oxidizing conditions. Sample surface area was determined by measuring the dimensions of the sample along three perpendicular directions; we used these to construct an ellipsoidal representation of the sample.

5.2. Experimental Procedure

Three different furnaces were used for the experiments reported below, each corresponding to a different pressure regime. The lowest pressure experiments ($P \approx 10^{-6}$ torr), which we will refer to as vacuum experiments, were carried out at the University of Chicago in a furnace designed and constructed by A. Hashimoto (see Hashimoto, 1990; Wang et al., 1999). The evaporation experiments run in hydrogen at a pressure of $\sim 2 \times 10^{-4}$ bar were carried out in a furnace at the University of Hokkaido. Details of this furnace are given in Hashimoto (1998) and in Kuroda and Hashimoto (2000a,b; 2002). An important consideration in the design of this furnace was to ensure that the hydrogen gas, before reaching the sample, equilibrates both in temperature and speciation. This is accomplished by flowing the hydrogen through tungsten granules and foil strips at the run temperature before allowing it to interact with the sample. The speciation of the hydrogen gas (H vs. H_2) is particularly important in that the species that has the far greater effect on the evaporation kinetics is monatomic hydrogen.

The experiments run at a total pressure of 1 bar were carried out in a gas-mixing Deltech tube furnace with a 1.25-inch inside diameter alumina muffle tube following the design given by Williams and Mullins (1976). The oxygen fugacity in the vicinity of the sample was controlled by flowing 600 $cm^3\ s^{-1}$ (STP) of $H_2 + CO_2$ mixtures through the furnace tube. The oxygen fugacity was monitored by a zirconia oxygen fugacity probe by using the calibration for very reducing conditions of Mendybaev et al. (1998).

5.3. Analytical Procedures

The starting materials and the evaporation residues were analyzed for major element composition with a JEOL JSM-5800LV scanning electron microscope equipped with an Oxford Link ISIS-300 energy-dispersive microanalytical system. The instrument was operated with an accelerating voltage of 15 kV and a beam current of 2 nA; synthetic and natural minerals were used as standards. Some evaporation residues formed crystals on quenching, and in some of the experiments performed at 1500°C in 2×10^{-4} bar H_2, melilite may have begun to crystallize at high degrees of evaporation. For these samples, several hundred spot analyses evenly spaced over the sample were done. All analyses were done with sums normalized to 100%. However, the software reports the counting statistics uncertainty in each analysis and spots that were in epoxy or cracks can easily be recognized on plots of concentration vs. uncertainty. After rejecting these analyses, estimates of the average composition were made. The magnesium isotopic measurements were made with a modified AEI IM-20 ion microprobe by means of methods described in Russell et al. (2000). CAI glasses from experiments run at 1 atm in air (which experienced no evaporation) were used as standards. Because there was no possibility of radiogenic ^{26}Mg from ^{26}Al decay in these samples, F_{Mg} was calculated from both magnesium isotope ratios: $F_{Mg} = 0.5\ \delta^{25}Mg_{sample} + 0.25\ \delta^{26}Mg_{sample}$, where $\delta^{25}Mg_{sample} = 1000\ [(^{25}Mg/^{24}Mg)_{sample}/(^{25}Mg/^{24}Mg)_{start} - 1]$ and $\delta^{26}Mg_{sample} = 1000\ [(^{26}Mg/^{24}Mg)_{sample}/(^{26}Mg/^{24}Mg)_{start} - 1]$.

We have focused our isotopic measurements of the evaporative residues on magnesium. The reason for this is a combination of our experience that the ion microprobe has better precision measuring magnesium isotopes than silicon isotopes, together with the expectation that magnesium isotopes will be significantly more fractionated than silicon isotopes in any given evaporation residue (see Fig. 1 in Davis et al., 1990).

6. RESULTS

We begin with a separate discussion of each set of experiments run under the different pressure conditions and, where possible, compare the results to previous experimental data, which is mainly for forsterite.

6.1. Vacuum Experiments

A total of 10 vacuum experiments ($P < 10^{-9}$ bar) are listed in Table 1, seven run with starting material B-133 and three with starting material B-113. Figure 2 shows how the SiO_2 and MgO contents of the B-133 series evolve as evaporation proceeds, and compares this to compositional trajectories calculated for different temperatures by using the thermodynamic model described in Grossman et al. (2000). The trajectories were calculated by using the ratio of the molar fluxes of silicon and magnesium as given by

$$\frac{J_{Si}}{J_{Mg}} = \frac{\gamma_{SiO}}{\gamma_{Mg}} \frac{P_{SiO}}{P_{Mg}} \sqrt{\frac{m_{Mg}}{m_{SiO}}}. \quad (11)$$

Eqn. 11 follows from Eqn. 2 given that the dominant gas species are Mg and SiO (according to our thermodynamic calculations, the next most abundant gas species, MgO and SiO_2, are less abundant by a factor of more than 100), and assuming that recondensation is negligible. The saturation vapor pressures of aluminum and calcium gas species are lower than those of magnesium and silicon by a factor of 10^5 or more, thus aluminum and calcium do not evaporate to any significant degree under the conditions of our experiments. Figure 2 shows a dramatic change in the relative evaporation rates of silicon and magnesium as evaporation proceeds. At the higher silica contents, silicon is lost much faster than magnesium, but once SiO_2 reaches ~35 wt% in the residue, SiO_2 and MgO decline at more or less the same rate. The evaporation rates of silicon and magnesium are proportional to the saturation vapor pressures of SiO and Mg respectively, which in turn reflect the activities of SiO_2 and MgO in the melt. Figure 3 shows the

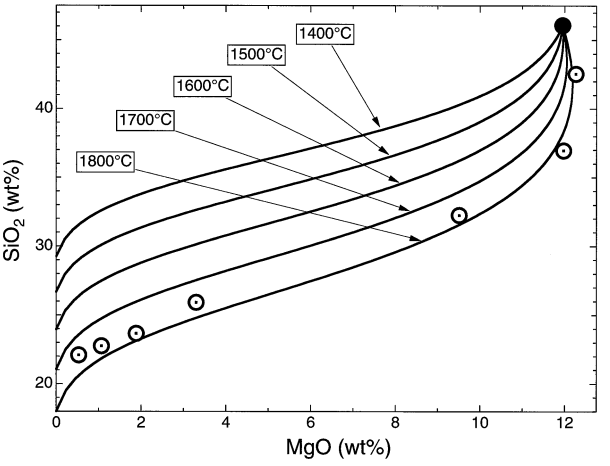

Fig. 2. Measured weight percentages of SiO_2 and MgO of the B-133 starting material (solid symbols) and evaporation residues (open symbols) from vacuum experiments run at 1800°C compared with calculated compositional trajectories for various temperatures. The compositional trajectories were calculated by Eqn. 11 with vapor pressures as a function of temperature and composition determined in the manner discussed in Grossman et al. (2000) and assuming that the evaporation coefficient of Mg and SiO are the same (i.e., $\gamma_{Mg} = \gamma_{SiO}$).

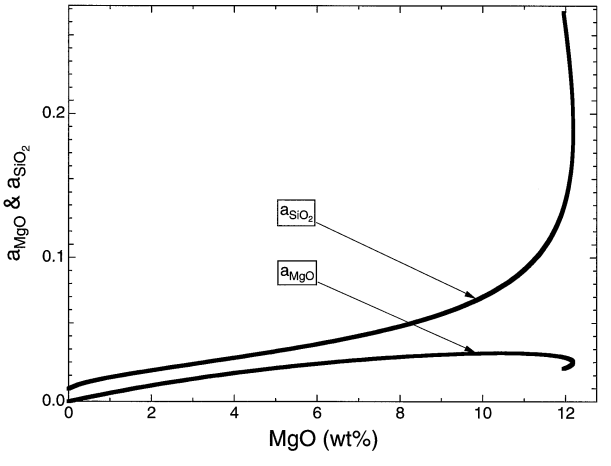

Fig. 3. Activity of MgO and SiO_2 as a function of weight percentage MgO for liquids along the 1800°C evaporation trajectory shown in Figure 2. The activities were calculated by using the thermodynamic model discussed by Grossman et al. (2000).

activities of SiO_2 and MgO in the melt, calculated by using the thermodynamic model of Berman (1983), as a function of the wt% MgO along the evaporation trajectory. As one would expect from the trajectories in composition space (Fig. 2), the activity of SiO_2 starts out much larger than that of MgO but then declines rapidly to become similar to it over the later portions of the evaporation history. The agreement shown in Figure 2 between the calculated trajectory and the experimental data is an important indication that the Berman (1983) activity model for CaO-MgO-Al_2O_3-SiO_2 liquids (as used by Grossman et al., 2000) gives for our purposes a good representation of the relative activities of SiO_2 and MgO in our experimental samples.

The temperature, run duration, sample composition, and surface area of the vacuum experiments listed in Table 1 provide the data for calculating the average evaporation rate for each experiment. Figure 4a shows the average evaporation rate of magnesium and silicon plotted against the final weight percentage MgO of the vacuum experiments run at 1800°C. The fluxes appear to depend to some degree on composition in the sense of a general decline in the average flux of silicon and an increase in the average flux of magnesium as more of the magnesium is evaporated. This dependence of the average fluxes on the amount of MgO lost is expected given how the activities of SiO_2 and MgO change with decreasing weight percentage of Mg (Fig. 3).

Figure 4b is a plot of calculated evaporation coefficients for SiO and Mg as a function of the final weight percentage of MgO of each run. The evaporation coefficients were calculated by using the relationship

$$\gamma_i = J_i \frac{\sqrt{2\pi m_i RT}}{P_{i,sat}}, \quad (12)$$

which follows from Eqn. 1 when there is a single dominant gas species for magnesium (Mg) and for silicon (SiO). For the systems of interest here, the saturation vapor pressures of Mg and SiO are two orders of magnitude or more larger than that of the next most important magnesium- and silicon-containing species in the gas. By using the experimentally determined net fluxes for J_i in Eqn. 12, we are implicitly ignoring the effect of recondensation. For $P_{i,sat}$ we use the average saturation vapor pressure over the duration of each experiment calculated along appropriate segments of compositional trajectories such as the one shown in Figure 2 for the B-133 samples. The evaporation coefficients are found to be significantly less than one (~0.2 to 0.1) and appear to depend on composition by being smallest for those samples that lost the least magnesium and silicon.

Figure 5 shows the isotopic fractionation of magnesium isotopes of the B-133 residues (in ‰ amu^{-1} relative to the starting composition) as a function of the fraction of magnesium evaporated. The dotted curve in this figure corresponds to Rayleigh fractionation calculated from Eqn. 5 with Mg as the dominant gas species, in which case $\alpha = \sqrt{24/25} = 0.97980$. The data fall noticeably below the calculated curve and are better fit by the solid curve corresponding to Rayleigh fractionation with $\alpha = 0.98921 \pm 0.00035$. There are several possible reasons why the measured fractionations are less than the expected value. It is possible, but in our opinion unlikely, that Mg is not the only significant gas species. Calculations for the

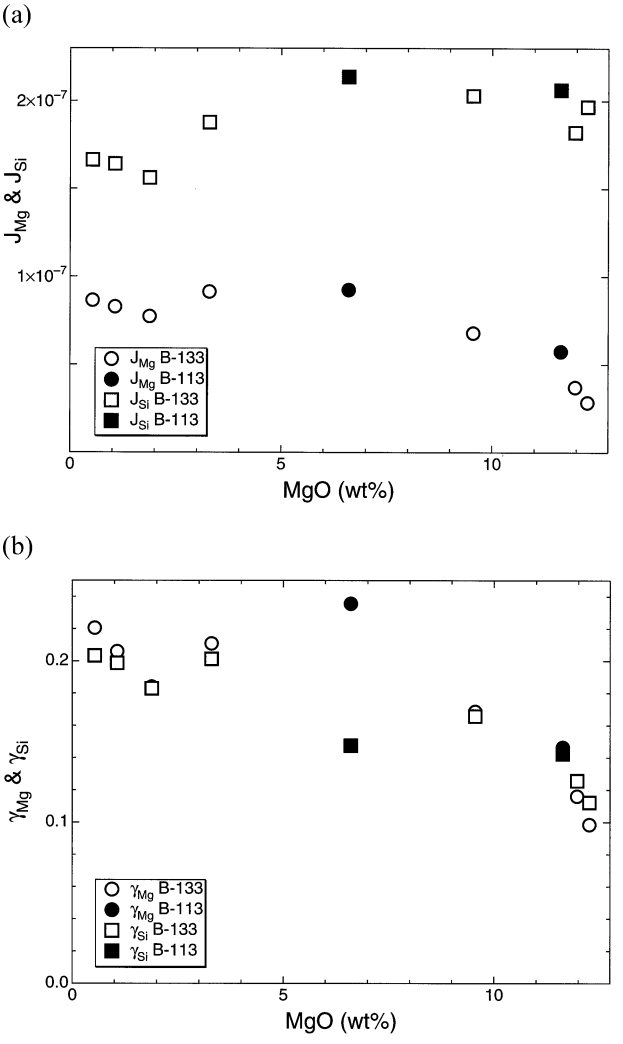

Fig. 4. (a) Average evaporation rate of magnesium and silicon in moles per unit surface area of sample per unit time (mol $cm^{-2}s^{-1}$) plotted against the final weight percentage MgO of the B-133 and B-113 samples run in vacuum at 1800°C. (b) Evaporation coefficient for Mg and SiO calculated by Eqn. 12 plotted against the final weight percentage MgO of the B-133 and B-113 samples run in vacuum at 1800°C.

speciation of magnesium in the gas at experimental conditions indicate that Mg exceeds MgO, the next most abundant species, by about a factor of one hundred, whereas $\alpha = 0.98687$ would require that virtually all the magnesium in the gas be in the form of MgO. Another possible explanation is that recondensation affected the experiments and reduced the isotopic fractionation. We will show in section 7 that the effect of recondensation on isotopic fractionation can be approximated by an effective fractionation factor α' related to the original α by

$$\alpha' - 1 \approx (\alpha - 1)\left(1 - \frac{P_i}{P_{i,sat}}\right), \quad (13)$$

where P_i refers to the pressure of the evaporating species at the evaporating surface and $P_{i,sat}$ is the saturation vapor pressure of i with respect to that surface. According to Eqn. 13, a recondensation flux of ~35% of the free evaporation flux could

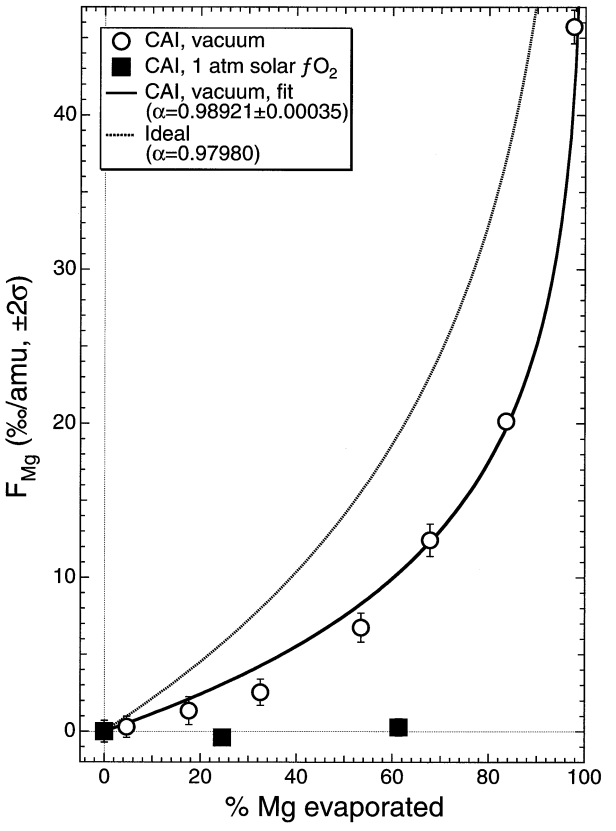

Fig. 5. Magnesium isotope fractionation of evaporation residues (‰ amu^{-1}) relative to the starting composition plotted against the percentage of Mg evaporated. Data are from B-133 and B-113 vacuum evaporation residues (circles) and B-113 samples run in 1-bar solar f_{O_2} (solid squares). The dotted curve is the Mg isotope fractionation calculated from Eqn. 5 with $\alpha = \sqrt{24/25} = 0.97980$. The solid curve is the best fit through the B-133 data and corresponds to $\alpha = 0.98921 \pm 0.00035$.

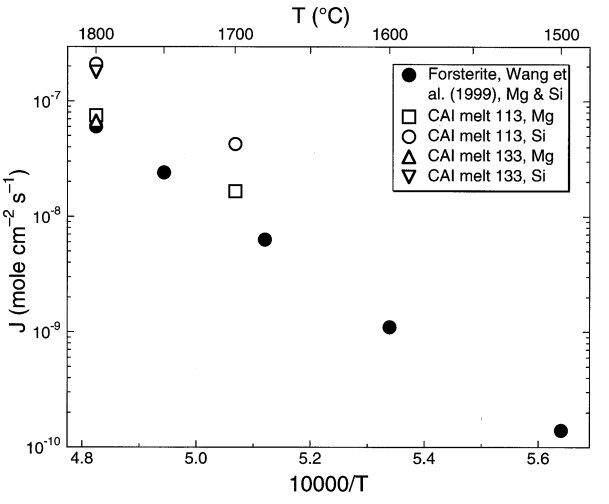

Fig. 6. Measured vacuum evaporation rates of single crystal forsterite (Wang et al., 1999) and two Type B CAI-like compositions (open symbols) plotted against temperature (°C in upper scale, K in bottom scale). Because forsterite evaporates stoichiometrically, its molar evaporation rates for magnesium and silicon are the same.

account for the lower than expected isotopic fractionation of magnesium in the B-133 residues. In the earlier discussion of evaporation rates and evaporation coefficients, we assumed that we could ignore recondensation and used the measured evaporation rates as estimates of the free evaporation rate J_i in Eqn. 12. If 35% recondensation did indeed occur in the experiments, then both the free evaporation rates and the evaporation coefficients are ~1.5 times larger than the values reported in Table 1 and plotted in Figures 4a,b. We should, however, emphasize that we have no independent evidence that something of the order of 35% recondensation did actually occur in our vacuum experiments. Yet another possibility is that the isotopic fractionation factor was affected by lack of sample homogeneity during evaporation. In this connection, we analyzed the quenched evaporation residues for chemical and isotopic gradients, and found none, which indicates that the samples are all sufficiently small for diffusion to maintain their homogeneity. We conclude from this that the departure of α from the theoretically expected value is not due to diffusion-limited evaporation of the sort discussed in section 8.

The most detailed previous studies of the evaporation kinetics of silicate material for cosmochemical purposes involved forsterite (e.g., Hashimoto, 1990; Wang et al., 1999; and references therein) or molten mixtures of FeO-MgO-SiO_2-CaO-Al_2O_3 (Hashimoto, 1983; Wang et al., 2001). Figure 6 compares the measured vacuum evaporation rates from Type B CAI-like liquids to the rates determined by Wang et al. (1999) for single crystal forsterite. Forsterite evaporation is stoichiometric, whereas the B-133 and B-113 melt compositions have silicon evaporation rates about three times larger than that of magnesium. This difference aside, the evaporation rates shown in Figure 6 are remarkably similar considering that we are comparing different compositions and that the forsterite samples were solid whereas the Type B CAI-like compositions were liquid. The similarity includes the dependence on temperature, which corresponds to an activation energy of ~625 kJ mol^{-1} for the forsterite data and ~525 kJ mol^{-1} for both silicon and magnesium in the B-113 series data. The magnesium and silicon evaporation rates determined by Wang et al. (2001) for molten mixtures of FeO-MgO-SiO_2-CaO-Al_2O_3 fall along the high-temperature extension of the data plotted in Figure 6. In the case of forsterite and the B-113 composition, the measured activation energies are ~100 kJ mol^{-1} larger than the value calculated from thermodynamic data. This difference between measured and calculated activation energies will translate into a temperature dependence of the evaporation coefficients.

6.2. Experiments with $P_{H_2} \approx 2 \times 10^{-4}$ bar

Six evaporation experiments run at T = 1500°C and $P_{H_2} = 1.87 \times 10^{-4}$ bar with BCAI-0 as the starting composition are listed in Table 1. These experiments are further subdivided on the basis of the size, with the SS-, S- and M- series having starting masses of ~5, ~17, and ~68 mg, respectively. Figure 7 compares the weight percentage of SiO_2 and MgO of the evaporation residues of the BCAI series with compositional trajectories calculated by using the thermodynamic model of

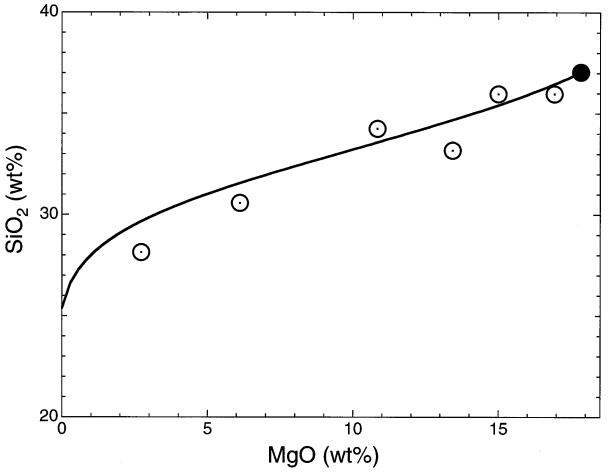

Fig. 7. Measured weight percentages of SiO_2 and MgO of the BCAI-0 starting material and evaporation residues from experiments run in 1.87×10^{-4} bar H_2 and T = 1500°C compared with the calculated compositional trajectories for T = 1500°C. The compositional trajectories were calculated assuming that the evaporation rates of magnesium and silicon are proportional to the equilibrium vapor pressures of Mg and SiO as calculated by the thermodynamic model of Grossman et al. (2000).

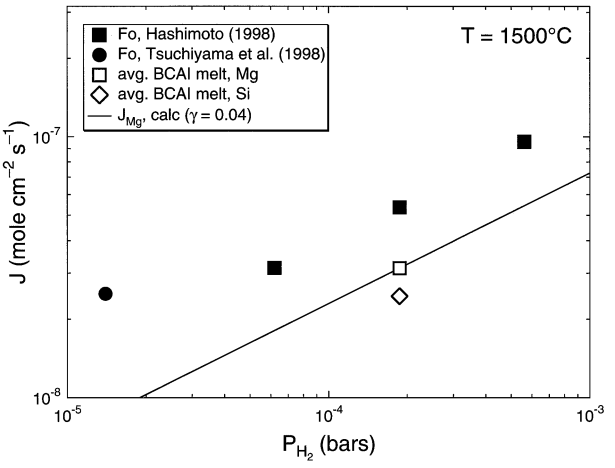

Fig. 8. Evaporation rate as a function of hydrogen pressure of forsterite from Hashimoto (1998), Tsuchiyama et al. (1998), and the average of the BCAI composition melts listed in Table 1. The straight line is the calculated evaporation rate of magnesium from the BCAI composition by Eqn. 1, where the saturation vapor pressure of Mg, the only significant magnesium-bearing gas-phase species, is calculated by using the thermodynamic model described in Grossman et al. (2000). An evaporation coefficient $\gamma = 0.04$ was used in order that the calculated evaporation rate fall through the average measured magnesium evaporation rate of the BCAI samples.

Grossman et al. (2000). The BCAI trajectory shown in Figure 7 was calculated assuming that the evaporation of Mg relative to SiO is in proportion to the ratio of their saturation vapor pressures, and therefore that the evaporation coefficients differ by an amount equal to the square root of the ratio of the mass of the evaporating species (see Eqn. 11). Because of the furnace used, the BCAI samples cooled sufficiently slowly that discrete minerals crystallized, which makes the determination of their bulk composition somewhat more uncertain than for residues quenched to glass. Given these uncertainties and the associated scatter of the data in Figure 7 around the calculated compositional trajectory, small differences between the evaporation coefficients of Mg and SiO of the order of the ratio of the square root of the respective masses are not really resolved.

Figure 8 compares the rates of evaporation of magnesium and silicon from the BCAI series samples to published data for forsterite under similar conditions of temperature and hydrogen pressure (Hashimoto, 1998; Tsuchiyama et al., 1998) and shows that the evaporation rates of Type B CAI-like liquids are, again, very similar to that of forsterite. Comparing the T = 1500°C evaporation rate from Figure 6 with the data in Figure 8 shows that the evaporation rates at comparable temperatures are more than two orders of magnitude faster in $\sim 10^{-4}$ bar hydrogen than in vacuum (see also Nagahara and Ozawa, 1996; and fig. 6 in Tsuchiyama et al., 1998). Hashimoto's (1998) forsterite data in Figure 8 fall along a line with slope $\sqrt{P_{H_2}}$, which corresponds to the thermodynamically predicted dependence of the saturation vapor pressure on P_{H_2}. The data point in Figure 8 attributed to Tsuchiyama et al. (1998) is extrapolated from their reported value at T = 1450°C using their reported activation energy. This data point is somewhat higher than would be expected from the extrapolation of Hashimoto's data to $P_{H_2} = 1.4 \times 10^{-5}$ bar. We believe the most likely reason for this discrepancy is that Tsuchiyama et al. (1998) underestimated the actual pressure in the vicinity of the evaporating sample by about a factor of 10 (see Kuroda and Hashimoto, 2000, 2001a,b, for a detailed discussion of this point). We expect that the evaporation of magnesium and silicon from Type B CAI-like liquids will depend on hydrogen pressure in the same way as forsterite on the basis of our thermodynamic calculations showing that the saturation vapor pressures of Mg and SiO over Type B CAI-like liquids increase with hydrogen pressure as $\sqrt{P_{H_2}}$. The line in Figure 8 is the evaporation rate of magnesium calculated by using the saturation vapor pressure from the Grossman et al. (2000) thermodynamic model in Eqn. 1 with $\gamma_{Mg} = 0.04$.

Tsuchiyama et al. (1998) report an activation energy for forsterite evaporation in 1.4×10^{-5} bar H_2 (actually closer to 10^{-4} bar by our estimate) of 372 kJ mol^{-1}, which is significantly smaller than the activation energy measured in vacuum experiments ($\sim$625 kJ mol^{-1}). Such a decrease in the activation energy when hydrogen is present is consistent with thermodynamic calculations for vapor pressures over forsterite that give $\sim$500 kJ mol^{-1} for vacuum evaporation and only $\sim$250 kJ mol^{-1} for $P_{H_2} \sim 10^{-4}$ bar. However, both in vacuum and in hydrogen, the experimentally measured activation energy for forsterite evaporation is $\sim$100 kJ mol^{-1} larger than the value calculated from thermodynamic data. In the case of the BCAI composition, we were not able run evaporation experiments at temperatures sufficiently above or below 1500°C to allow us to determine an activation energy. The reason is that the particular furnace used for evaporations in hydrogen has an upper temperature limit of 1500°C, and experiments run at significantly lower temperatures will partially crystallize during the experiment. Thermodynamic calculations that use the Grossman et al. (2000) model give an activation energy of $\sim$200 kJ mol^{-1} for evaporation of the BCAI composition in 1.87×10^{-4} bar H_2. Given that the measured activation energies for evaporation of

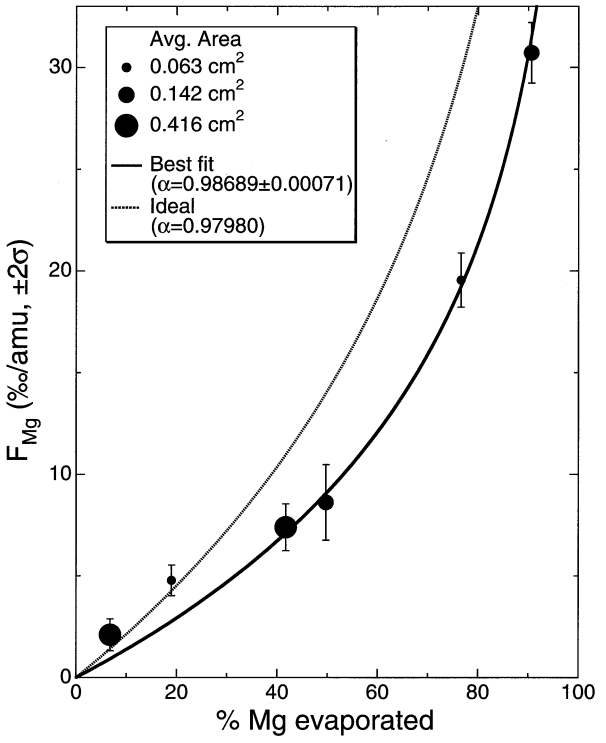

Fig. 9. Magnesium isotopic fractionation of BCAI evaporation residues (‰ amu^{-1}) relative to the starting composition plotted against the percentage of Mg evaporated. The dotted curve is the magnesium isotope fractionation calculated from Eqn. 5 with $\alpha = \sqrt{24/25} = 0.97980$. The solid curve is the best fit through the BCAI data and corresponds to $\alpha = 0.98689 \pm 0.00071$. The BCAI samples were intentionally made to have a range of surface areas, and these are indicated in the figure by different-sized symbols. The data do not resolve any dependence of the isotopic fractionation on sample size.

forsterite and B-113 samples in vacuum, and for forsterite in 1.4×10^{-5} bar H_2, are always ~100 kJ mol^{-1} larger than the corresponding thermodynamically calculated value, it seems reasonable to assume that the activation energy for evaporation of the BCAI composition in 1.87×10^{-4} bar H_2 is also ~100 kJ mol^{-1} larger than the calculated value. In later discussions, we will use an activation energy of 300 kJ mol^{-1} for the evaporation of Type B CAI-like liquids whenever there is sufficient hydrogen present to significantly enhance the evaporation rates.

The isotopic fractionation associated with the evaporation of magnesium from the BCAI series samples is shown in Figure 9. As seen earlier for the B-133 residues, the data show Rayleigh fractionation-like behavior, but with a fractionation factor $\alpha = 0.98689 \pm 0.00071$ rather than the expected value for magnesium of $\alpha = 0.97980$. We mentioned earlier that recondensation is a possible reason that the measured isotopic fractionations of the evaporation residues are somewhat less than the theoretically expected value. The BCAI experiments were designed to assess the role of recondensation by using samples with a range of surface areas from 0.063 to 0.416 cm^2. Given the design of the furnace used for these experiments, the expectation was that the larger the sample surface area, the greater the recondensation per unit surface area. The sample chamber of the hydrogen furnace consists of a large cylindrical cavity into which H_2 gas flows at a controlled rate F_{H_2} and leaves via a small diameter cylindrical tube of known gas conductance U connected to vacuum at its far end. The P_{H_2} in the sample chamber is determined by the pressure change due to the flow through the cylinder of conductance U. Thus $P_{H_2} = F_{H_2}/U$. A similar relationship will hold for all other gas species i in the sample chamber, but in their cases the fluxes F_i will be due to evaporation. Thus $F_i = AJ_{i,net}$ where A is the surface area of the sample. Because the sample chamber conductance for species i is proportional to that for hydrogen, $P_i \approx AJ_{i,net}/U$, and so $P_i/P_{i,sat} \rightarrow 0$ as $A \rightarrow 0$ and recondensation should go to zero as $A \rightarrow 0$. It follows that the smaller the sample, the less important recondensation should be, and the closer α should be to the theoretically expected value. To our surprise, we found no significant difference in the magnesium isotopic fractionation behavior of the BCAI samples as a function of their surface area. This can be seen in Figure 9, where all samples with more than 20% Mg loss lie within error on a common fractionation curve implying a common value of α. We have no good explanation as to why we keep finding the same value for α that is different from the theoretically expected value. We note, again without explanation, that the values of α for Mg (on a ‰ amu^{-1} basis) reported by Wang et al. (1999, 2001) for solid forsterite (vacuum, $\alpha = 0.986$) and for their molten solar composition (vacuum, $\alpha = 0.985$), and by Davis et al. (1990) for molten forsterite (vacuum, $\alpha = 0.985$), are all very similar to the value we find for the Type B–like liquids (vacuum and 1.87×10^{-4} bar H_2, $\alpha = 0.989$ and 0.987, respectively) rather than the theoretically expected value ($\alpha = 0.980$).

6.3. Experiments with $P_{H_2} \approx 1$ bar

Two of the B-113 series experiments listed in Table 1 were carried out in a gas-mixing Deltech furnace containing extremely reducing $H_2 + CO_2$ mixtures at a total pressure of 1 bar. The oxygen fugacity was set to that of a solar gas (log $f_{O_2} \approx -16.5$ at T = 1400°C) by adjusting the ratio of H_2 to CO_2 and monitored with a zirconia oxygen fugacity probe as described by Mendybaev et al. (1998). The mass loss rates and element fractionations measured in the residues of the 1-bar experiments are almost certainly the result of a near-equilibrium process (i.e., $P_i/P_{i,sat} \approx 1$) and thus only indirectly related to the evaporation kinetics discussed above. According to Eqn. 3, $J_{i,net} \approx 0$ when $P_i/P_{i,sat} \approx 1$—that is, no net evaporation and thus no elemental or isotopic fractionation occur. This would be the case in a closed system, but our 1-bar experiments were carried out in an open system with gas flowing through the furnace to control the oxygen fugacity. The samples do lose silicon and magnesium because of the continuous removal of gas containing silicon and magnesium. The partial pressures of calcium and aluminum in the gas are so low that their mass loss is negligible over the duration of the experiments. A further indication that the 1-bar experiments are very near equilibrium is given by the fact that the residues are not fractionated in magnesium isotopes even when as much as 60% of the initial magnesium has been lost (see Table 1 and Fig. 5). We interpret the lack of measurable isotopic fractionation as being due to $P_{i,}/P_{i,sat} \approx 1$, which according to Eqn. 13, results in an effective fractionation factor $\alpha' \approx 1$ and thus no significant isotope fractionation. The 1-bar hydrogen experiments are consistent

with our expectations of the consequences of evaporation in the limit of high surrounding pressure.

7. PARAMETERIZATIONS FOR THE RATE AND CONSEQUENCES OF EVAPORATION

In this section, we develop various simple parameterizations for the evaporation of silicon and magnesium from molten Type B CAI-like compositions. Assuming that we are dealing with an element such as magnesium that has one dominant gas species and that we can ignore the far field gas pressure $P_{i,\infty}$ of the evaporating species, Eqn. 9 becomes

$$J_{i,net} = \frac{\gamma_i P_{i,sat}}{\sqrt{2\pi m_i RT}} \Big/ \left(1 + \frac{\gamma_i a}{D_i}\sqrt{\frac{RT}{2\pi m_i}}\right). \quad (14)$$

For a given temperature and composition, $P_{i,sat}$ should be calculated by using the same thermodynamic model used to determine the evaporation coefficient γ_i. Given an inclusion of radius a, the remaining quantities that need to be specified are the interdiffusion coefficient D_i of species i in the surrounding dominantly hydrogen gas and the evaporation coefficient $\gamma_{i,}$. The interdiffusion coefficient of i in a gas dominated by a species j (e.g., H_2) can be calculated from the expression

$$D_{ij} = \frac{0.002628}{P\sigma_{ij}^2\Omega_d}\sqrt{\frac{T^3(m_i + m_j)}{2m_i m_j}}. \quad (15)$$

D_{ij} will have units of square centimeters per second when P is the total gas pressure in bars, σ_{ij} (~3.5 Å) is the average of the individual collision diameters σ_i and σ_j in angstroms, Ω_d (~0.75) is the collision integral (a dimensionless measure of the departure from rigid sphere behavior), m_i and m_j are the molecular weights of i and j in grams, and T is the absolute temperature. By use of the above values for σ_{ij} and Ω_d, which were taken from Geankoplis (1962) and Balat et al. (1992), we find that for both Mg and SiO

$$D \approx \frac{0.00014}{P} T^{\frac{3}{2}}. \quad (16)$$

This approximate form for D is easily justified given realistic uncertainties in specifying an appropriate value for the pressure.

Evaporation coefficients determined by recent laboratory evaporation experiments using various silicate compositions, hydrogen pressures, and temperatures are shown in Figure 10. The evaporation coefficients have a significant temperature dependence, which could have been anticipated from the fact that forsterite, whether in vacuum or hydrogen, was found to have an effective activation energy somewhat larger than the thermodynamic value (Tsuchiyama et al., 1998; Wang et al., 1999). The evaporation coefficients for the Type B CAI-like compositions, whether in vacuum or in 1.87×10^{-4} bar hydrogen, are very similar in magnitude and temperature dependence to that of forsterite in vacuum. The evaporation coefficients calculated from Kuroda and Hashimoto's (2000a,b) data continue the trend with respect to temperature of the vacuum coefficients, while evaporation coefficients based on

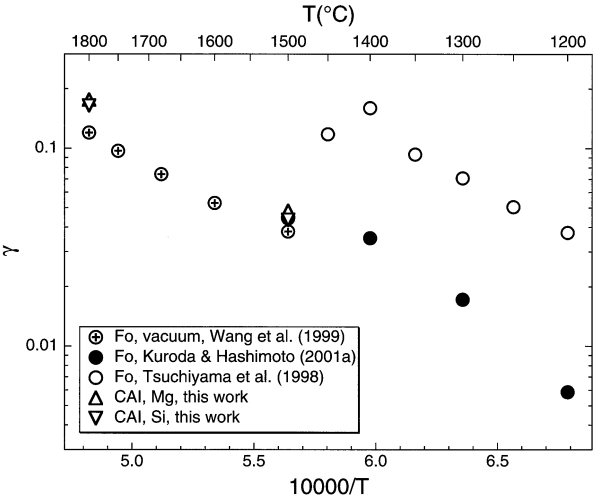

Fig. 10. Evaporation coefficients γ as a function of temperature for forsterite in vacuum (Wang et al., 1999), in 1.87×10^{-4} bar hydrogen (Kuroda and Hashimoto, 2000), and in 1.4×10^{-5} bar hydrogen (Tsuchiyama et al., 1998); and for Type B CAI-like compositions (this study). The CAI evaporation coefficients at T = 1800°C are the averages for the B-133 vacuum experiments while those at T = 1500°C are the averages for the BCAI experiments run in 1.87×10^{-4} bar hydrogen.

the Tsuchiyama et al. (1998) data fall significantly above this trend. As we noted earlier this is most likely due to Tsuchiyama et al. (1998) underestimating the actual hydrogen pressure in the vicinity of their evaporating samples. In terms of specifying evaporation coefficients for Type B CAIs, we will be most interested in temperatures near 1400°C and hydrogen pressures in the range 10^{-3} to 10^{-5} bar. A reasonable choice for the evaporation coefficient under these conditions is $\gamma_{Mg} = \gamma_{SiO} = 0.03$.

An experimentally validated representation for the evaporation of Type B CAI-like liquids is given by Eqn. 14 using the thermodynamic model of Grossman et al. (2000) for the required saturation vapor pressures, Eqn. 16 for the interdiffusion coefficient D, and Figure 10 for the evaporation coefficients. The effects of melt composition, temperature, gas composition, and pressure on the evaporation rate are taken into account by the calculated saturation vapor pressures. It should be kept in mind that the evaporation coefficients plotted in Figure 10 are defined with respect to the specific thermodynamic model used to calculate the saturation vapor pressures. Had we, for example, used an ideal solution model for the Type B CAI-like liquid, we could still determine evaporation coefficients, but they would be with respect to the saturation vapor pressures over the ideal solution. The penalty one would pay for using such an oversimplified solution model for the evaporating liquid is that all the deficiencies of the activity–composition relationships will complicate the dependence of the evaporation coefficients on composition. By using a realistic solution model for the CAI-like liquids, we find, as can be seen from Figure 10, that the evaporation coefficients of Mg and SiO are effectively the same and that they depend mainly on temperature. Effects due to sample composition, surrounding gas, and even whether the material is solid or liquid, are seen to be far less important than that of temperature.

An alternative representation for the evaporation kinetics can be made based on parameterizing the effects of temperature and pressure around the experimental results closest to the conditions of interest. When in the hydrogen dominated regime ($P_{H_2} > 10^{-7}$ bar for T < 1500°C), the evaporation flux of Type B CAI-like liquids at a temperature T and hydrogen pressure P can be calculated by using the following relationship:

$$J_i(T,P) = \frac{J_i(T_0,P_0)e^{\frac{-E}{R}\left(\frac{1}{T}-\frac{1}{T_0}\right)}\sqrt{\frac{P}{P_0}}}{1+\frac{\gamma a}{D}\sqrt{\frac{RT}{2\pi m_i}}}. \quad (17)$$

$J_i(T_0,P_0)$ is the experimentally determined evaporation rate at temperature T_0 and H_2 pressure P_0 and E is the activation energy. Specifying the effect of hydrogen pressure as being proportional to $\sqrt{P/P_0}$ is justified by both the forsterite experimental data and the calculated evaporation rate for CAI-like compositions shown in Figure 8. Our best estimate for the effective activation energy E for a Type B CAI-like liquid is 300 kJ mol^{-1}, which is ~100 kJ mol^{-1} larger than the value given by our thermodynamic calculation. The extra 100 kJ mol^{-1} assumes that when hydrogen is present there is a similar difference between the calculated and measured activation energy for the CAI-like liquid as we found in our vacuum evaporations of CAI-like liquids and as has been found for evaporation of forsterite in both vacuum and in hydrogen gas (Tsuchiyama et al., 1998; Wang et al., 1999; Kuroda and Hashimoto, 2000, 2001a,b). The 100 kJ mol^{-1} difference between the calculated and measured activation energy shows up as the temperature dependence of the evaporation coefficients shown in Figure 10. By incorporating the 100 kJ mol^{-1} into an effective activation energy, we can use a fixed value, $\gamma = 0.03$, for the evaporation coefficient.

A more general parameterization, not restricted to the hydrogen-dominated regime and thus valid to lower pressures than Eqn. 17, results when we rewrite Eqn. 17 in terms of oxygen fugacity (P_{O_2}) rather than P_{H_2}:

$$J_i(T,P_{O_2}) = \frac{J_i(T_0,P_0)e^{\frac{-E_0}{R}\left(\frac{1}{T}-\frac{1}{T_0}\right)}\sqrt{\frac{P_0}{P_{O_2}}}}{1+\frac{\gamma a}{D}\sqrt{\frac{RT}{2\pi m_i}}}, \quad (18)$$

where P_0 now refers to a reference oxygen fugacity and E_0 is the effective activation energy keeping P_{O_2} fixed. The surrounding gas composition and pressure still need to be specified to calculate the interdiffusion coefficient of species i in the surrounding gas via Eqn. 15. Figure 11a shows the calculated evaporation rates of magnesium as a function of P_{O_2} for three different temperatures by using the thermodynamic model of Grossman et al. (2000). Both O and O_2 can be significant species, depending on conditions. We chose to parameterize P_{O_2}, because P_O is proportional to $\sqrt{P_{O_2}}$ and P_{O_2} is a quantity measurable with a sensor in a laboratory experiment. The temperature dependence of the evaporation rate corresponds to an activation energy at fixed f_{O_2} of $E_0 \approx 650$ kJ mol^{-1}. The relationship between P_{O_2} and P_{H_2} in the calculations used to construct Figure 11a is shown in Figure 11b and corresponds to the situation when the oxygen fugacity is controlled by equilibrating the molten sample with a surrounding gas initially containing only hydrogen at the specified P_{H_2}. In the hydrogen-dominated regime ($P_{H_2} > 10^{-8}$ bar) P_{O_2} is a linear function of P_{H_2}, which accounts for Eqns. 17 and 18 being equally valid in this regime. The linear relationship breaks down at lower P_{H_2}, once the amount of oxygen tied up by hydrogen (mostly as H_2O) becomes a small part of the oxygen budget, with the effect that Eqn. 17 no longer holds (but Eqn. 18 still does). Also shown in Figure 11b are curves of P_{O_2} vs. P_{H_2} for a gas of solar composition at various temperatures. At sufficiently high pressure the oxygen fugacity around a molten Type B CAI-like liquid evaporating into a solar composition gas will be set by the solar gas and thus the P_{O_2} of the solar gas should be used in Eqn. 18.

Figure 12 summarizes various effects of hydrogen pressure on the evaporation rate from a Type B CAI-like composition at T = 1500°C. The heavy curve is calculated from Eqn. 14 by using Grossman et al. (2000) for the saturation vapor pressure of Mg in the gas over the BCAI composition and an evaporation coefficient $\gamma_{Mg} = 0.04$ in the limit radius $a \rightarrow 0$ (i.e., no recondensation). This value for the evaporation coefficient was chosen so that the calculated curve passes through the average evaporation rate of magnesium measured for samples of the BCAI series. The thinner curves were calculated by Eqn. 14 for three choices of the radius of the model sample (a = 0.2, 0.5, and 1.0 cm) and with the diffusivity D given by Eqn. 16. Three regimes are seen. When $P_{H_2} < 10^{-7}$ bar, the evaporation rate is independent of the hydrogen pressure and can be described as the vacuum regime. For P_{H_2} between 10^{-7} bar and $\sim 10^{-3}$ bar, the evaporation rate increases as $\sqrt{P_{H_2}}$, which is a hydrogen-dominated regime. At hydrogen pressures greater than $\sim 10^{-3}$ bar the interdiffusion of Mg through the surrounding gas becomes sufficiently slowed that the Mg pressure begins to build up on the surface of the sample and, as a result, recondensation starts to become important. The example given in Figure 12 is for a temperature of 1500°C. The regime boundaries do shift with temperature such that at lower temperatures the hydrogen-dominated regime extends to lower pressure (e.g., to $P_{H_2} \sim 10^{-8}$ bar at T = 1400°C, $P_{H_2} \sim 10^{-9}$ bar at T = 1300°C). The pressure at which recondensation begins to be important also decreases with decreasing temperature, but only slightly (i.e., a decrease of ~10% between 1500 and 1300°C).

We stated without proof in section 6.1 that the effect of recondensation on the isotopic fractionation of the residue can be represented by an effective fractionation factor α', which, to a reasonable approximation, is related to the free evaporation fractionation factor α by Eqn. 13. We now use Eqn. 14 to derive a more complete equation for the effective isotopic fractionation factor. Eqn. 14 for isotope k of element i can be written as

$$J_{i,k} = \frac{\frac{\gamma_i X_k P_{i,sat}}{\sqrt{2\pi m_k RT}}}{1+\frac{\gamma_i a}{D_{i,k}}\sqrt{\frac{RT}{2\pi m_k}}}, \quad (19)$$

where X_k is the mole fraction of isotope k in the evaporating material. Eqn. 19 implicitly assumes that there is no equilibrium isotope fractionation (valid at sufficiently high temperature) in that the equilibrium vapor pressure of k is written as X_k

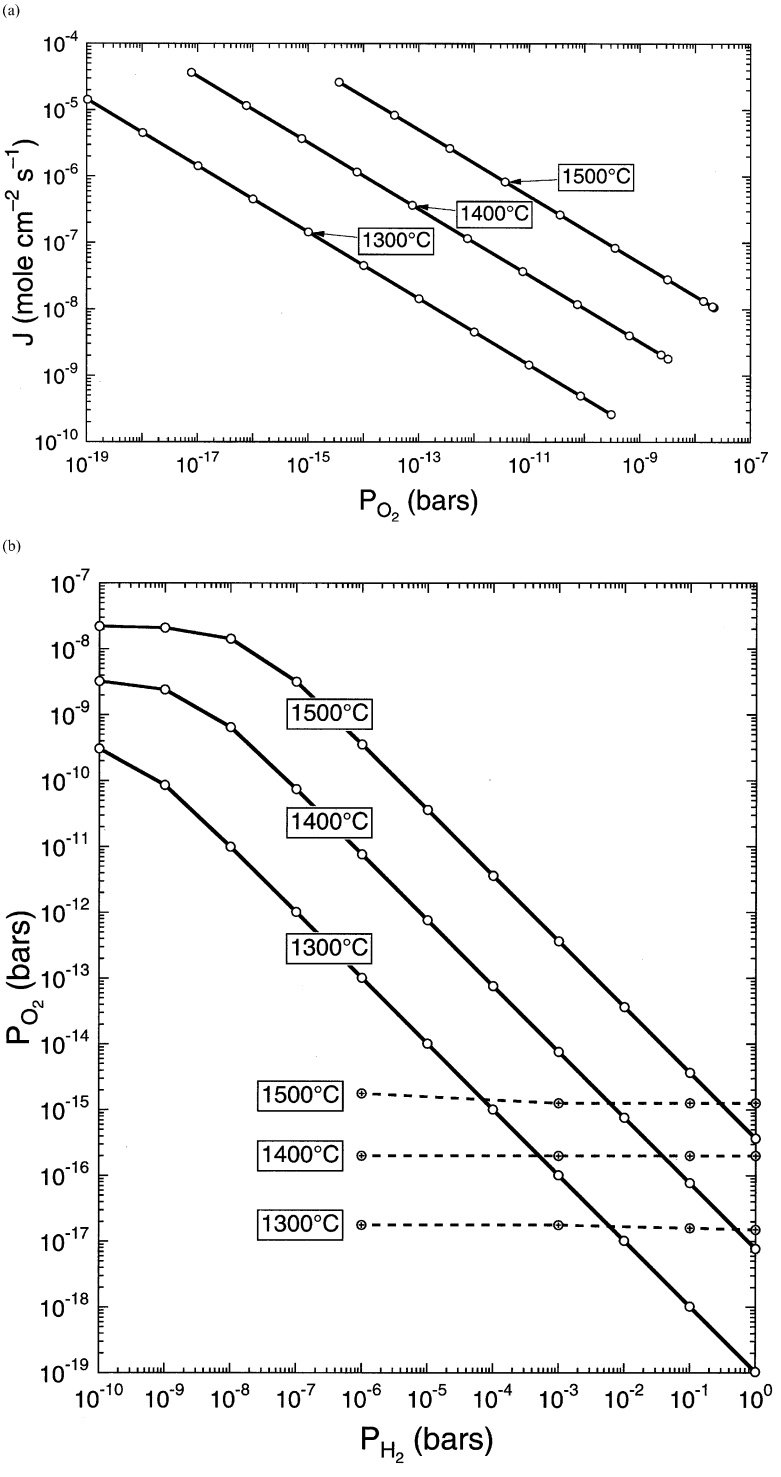

Fig. 11. (a) Dependence of the magnesium evaporation rate on P_{O_2} for the three temperatures indicated. The evaporation rate was calculated from Eqn. 1 assuming Mg as only important gas species, $\gamma = 1$, and $P_{Mg,sat}$ calculated by using the thermodynamic model of Grossman et al. (2000). The curves have slope $-\sqrt{P_{O_2}}$. (b) The solid curves show the P_{O_2} of the gas in equilibrium with a Type B CAI liquid at the indicated temperatures as a function of an imposed hydrogen pressure. The dashed curves show the oxygen fugacity, P_{O_2}, of a gas of solar composition at the three indicated temperatures. Three regimes are seen in this figure. At sufficiently low hydrogen pressures (the vacuum regime), the P_{O_2} tends to an asymptotic value depending only on the composition of the condensed material and temperature. At intermediate hydrogen pressures (the hydrogen-dominated regime), the oxygen is still derived from the sample but now P_{O_2} decreases with increasing P_{H_2} because of the formation of water. What we can call the solar composition-dominated regime corresponds to those situations where the P_{O_2} of the solar gas exceeds the P_{O_2} that would result from the equilibrium of the condensed phase with just hydrogen, in which case the P_{O_2} is set by the pressure and temperature of the solar gas.

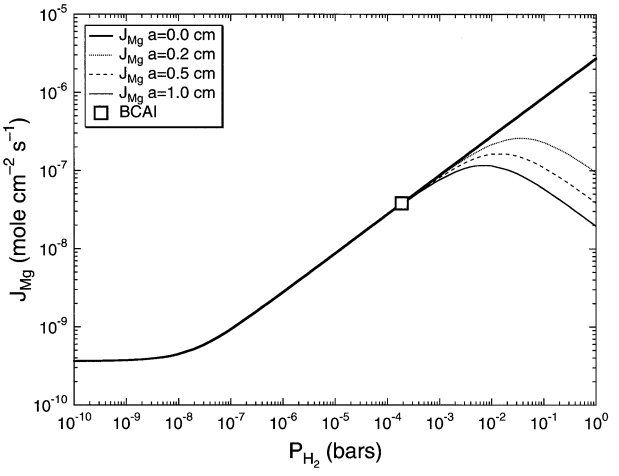

Fig. 12. Evaporation rate of magnesium at 1500°C vs. P_{H_2} showing the various effects of hydrogen on the evaporation rate. The heavy curve was calculated by Eqn. 14 with a = 0 (no recondensation), γ = 0.04 (in order that the curve pass through the average magnesium evaporation rate of the BCAI samples), and saturation vapor pressures calculated by using the model of Grossman et al. (2000). The three thinner curves show the effect of recondensation for CAIs of radius 0.2, 0.5, and 1.0 cm. Three regimes are seen. At sufficiently low hydrogen pressure (the vacuum regime), the evaporation rate is independent of P_{H_2}. In the hydrogen-dominated regime ($10^{-7} < P_{H_2} < 10^{-3}$ bar for T = 1500°C and r ≤ 1 cm), the evaporation rate increases as $\sqrt{P_{H_2}}$. At sufficiently high hydrogen pressure ($P > 10^{-3}$ bar for T = 1500°C), recondensation effects first reduce, then reverse the dependence of the evaporation rate on P_{H_2}. For $P_{H_2} > 10^{-7}$, the curves shown in this figure could have equally well been calculated by Eqn. 17, which does not require a thermodynamic model for calculating saturation vapor pressures. A similar figure for forsterite evaporation was presented by Hashimoto (1999).

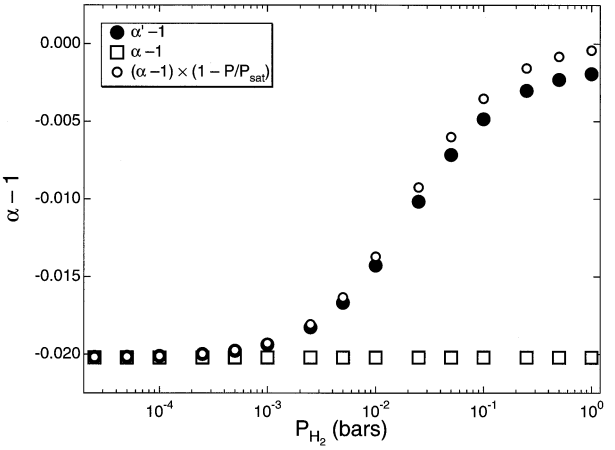

Fig. 13. Effect of recondensation on the effective kinetic isotope fractionation factor shown as the variation of $\alpha - 1$ vs. hydrogen pressure. The open-square symbols indicate the fractionation factor for $^{25}Mg/^{24}Mg$ in the absence of recondensation ($\alpha - 1 = \sqrt{24/25} - 1 = -0.0202$). The solid circles indicate the result calculated by Eqn. 22 and show that the asymptotic value of α in a saturated system is not one (no fractionation) but becomes equal to the ratio of the interdiffusion coefficients of the isotopes. The open circles are the result calculated by using the approximate form given by Eqn. 13.

times the saturation vapor pressure of the element. We also assume a common evaporation coefficient γ_i for all isotopes of i. The instantaneous ratio of isotope 1 to isotope 2 in the evaporating gas (R_g) is then given by

$$R_g = \frac{J_{i,1}}{J_{i,2}} = \frac{X_1}{X_2}\sqrt{\frac{m_2}{m_1}}\frac{\left[1+\frac{\gamma_i a}{D_{i,2}}\sqrt{\frac{RT}{2\pi m_2}}\right]}{\left[1+\frac{\gamma_j a}{D_{i,1}}\sqrt{\frac{RT}{2\pi m_i}}\right]}$$

$$= R_c\alpha\frac{\left[1+\frac{\gamma_j a}{D_{i,2}}\sqrt{\frac{RT}{2\pi m_2}}\right]}{\left[1+\frac{\gamma_j a}{D_{i,1}}\sqrt{\frac{RT}{2\pi m_i}}\right]} = R_c\alpha', \quad (20)$$

where R_c is the isotopic composition of the evaporating condensed phase, $\alpha = \sqrt{m_2/m_1}$ is the kinetic isotopic fractionation factor in the absence of recondensation, and α' is the effective fractionation factor taking recondensation into account. The mass dependence of the diffusivities $D_{1,j}$ and $D_{2,j}$ of the isotopes in a dominantly H_2 gas are given by Eqn. 15 with m_j = 2. Comparing Eqn. 3 with Eqn. 9 shows that in the limit of no significant far field pressure ($P_{i,\infty} = 0$), the quantities $\{1 + (\gamma_i a/D_{i,k})\sqrt{RT/2\pi m_k}\}$ are related to the pressure at the evaporating surface by the relationship

$$1 - \frac{P_k}{P_{k,sat}} = \frac{1}{1+\frac{\gamma a}{D_{i,k}}\sqrt{\frac{RT}{2\pi m_k}}}, \quad (21)$$

Eqns. 20 and 21 can be combined to give the following simpler relationship between α and α':

$$\alpha' - 1 = (\alpha - 1)\left(1 - \frac{P_1}{P_{1,sat}}\right) + \left(\frac{D_{i,1}}{D_{i,2}} - 1\right)\frac{P_1}{P_{1,sat}}. \quad (22)$$

Eqn. 13 is now seen to be an approximation based on ignoring the small difference between the diffusivities of the isotopes in the surrounding gas and the even smaller difference between elemental $P_i/P_{i,sat}$ and isotopic $P_1/P_{1,sat}$. Figure 13 is a plot of α' for magnesium as function of P_{H_2}, showing that significant departures from ideal fractionation $\alpha' = \sqrt{m_2/m_1}$ occur at $P_{H_2} > 10^{-3}$ bar and that the effect of the second term on the right hand side of Eqn. 22 is relatively small.

8. DIFFUSION IN THE LIQUID

We now turn to questions of when and how diffusion in a molten spherical CAI will affect the evaporation behavior. The model problem we need to solve is governed by Eqn. 10, subject to the boundary conditions 10a and 10b. For simplicity, we will assume the system to be entirely molten at all times ($\phi = 1$, $\partial\phi/\partial t = 0$) and that both the diffusivities $D_{i,m}$ and evaporation rates $J_{i,net}$ are unchanging with time ($D_{i,m} = D_{i,0}$, $J_{i,net} = J_{i,0}$). The assumption that the net evaporation rate is not changing significantly with time will be more valid for magnesium than for silicon because P_{Mg}, and thus J_{Mg}, is not strongly dependent on melt composition as long as MgO > 5 wt% (Fig. 3). We write the remaining parts of Eqn. 10 in terms of the nondimensional variables $r' = r/r_0$, $a' = a/r_0$, $C_i' = C_{i,m}/C_{i,0}$, and $t' = (D_0/r_0^2)t$. r_0 is the initial radius, D_0 is a

reference diffusivity, and $C_{i,0}$ is the initial molar density, assumed to be uniform. Eqn. 10, after dropping primes, becomes

$$\frac{\partial C_i}{\partial t} = D_i \left(\frac{\partial^2 C_i}{\partial r^2} + \frac{2}{r} \frac{\partial C_i}{\partial r} \right), \tag{23}$$

with

$$\frac{\partial C_i}{\partial r} = -\frac{J_{i,0} r_0}{C_{i,0} D_{i,0}} - \left(\frac{C_i}{D_i} \right) \frac{\partial a}{\partial t} \text{ at } r = a(t),$$

$$= -\frac{E_{vi}}{3} + \left(\frac{C_i}{D_i} \right) \sum \frac{E_{vj} V_j D_j}{3}, \tag{23a}$$

$$\frac{\partial C_i}{\partial r} = 0 \text{ at } r = 0, \tag{23b}$$

and with the initial condition $C_i(t,r) = 1$. In Eqn. 23a we used

$$\frac{\partial a}{\partial t} = -\sum \frac{E_{vj} V_j D_j}{3} \tag{23c}$$

The system is governed by the nondimensional quantities $D_i \equiv D_{i,0}/D_0$ (similarly for D_j) the evaporation number $E_{vj} \equiv (3J_{j,0}r_0/C_{j,0}D_{j,0})$, and the volume fraction of species j in the melt given by $V_j \equiv C_{j,0}\nu_j$, where ν_j is the molar volume of species j. E_{vj} corresponds to the ratio of the diffusive time scale ($\tau_{diff} = r_0^2/D_{j,0}$) to the evaporation time scale ($\tau_{evap} = (4/3)\pi r_0^3 C_{j,0}/4\pi r_0^2 J_{j,0} = r_0 C_{j,0}/3J_{j,0}$). We can anticipate that when the evaporation number is large, which corresponds to evaporation being fast relative to the diffusive adjustment time, significant radial concentration gradients will result. In the case of small evaporation numbers, diffusion will maintain nearly homogeneous concentrations, which is the condition required for Rayleigh fractionation.

Eqn. 23 for CaO, Al_2O_3, SiO_2, ^{24}MgO,^{25}MgO, and ^{26}MgO with the boundary condition (Eqn. 23a) applied at a radius calculated from Eqn. 23c were solved by numerical methods whose accuracy was demonstrated by comparison with analytical solutions for special cases (e.g., surface flux condition applied at a fixed radius or at a moving boundary of a half-space). Figure 14a shows solutions to Eqn. 23 in terms of the wt% of the oxides as a function of nondimensional radius r/r_0 after 50% of the magnesium has been evaporated for $E_{vMg} = 3$ (see caption for the other parameters). The concentration profiles reflect two opposing effects arising from the two terms on the right hand side of boundary condition 23a. Evaporation from the surface reduces the molar density of the evaporating species as the surface is approached while the decreasing radius tends to increase the molar density of the less rapidly evaporating components toward the surface. The MgO profile is dominated by evaporation while the profiles of the conserved species CaO and Al_2O_3 reflect the increase in their molar density as the radius and thus volume of the sample decreases. The SiO_2 profile is relatively flat because the effect of evaporation is almost perfectly balanced by that of changing radius for the particular set of parameters used. In the special case of congruent evaporation (e.g., evaporation of forsterite) the two terms on the right hand side of boundary condition in Eqn. 23a cancel exactly, and thus evaporation produces no change in the molar density (which is as it must be when the evaporation is congruent).

Figure 14b shows the effect of the evaporation number on the MgO profile after 50% of the MgO has evaporated. As expected, gradients are weak for $E_v < 1$ and significant for $E_v > 1$. Once E_v exceeds 10, the center of the inclusion has hardly lost any MgO even though the model system as a whole has lost 50% of its starting MgO content. For $E_v > 10$, concentration gradients are restricted to a near surface diffusive boundary layer. Figure 14c shows the magnesium isotopic composition profiles associated with the compositional profiles shown in Figure 14b. The relative evaporation flux of the magnesium isotopes was assumed to be proportional to the magnesium isotopic ratio at the surface times the inverse of the square roots of their masses (Eqn. 4b). We ignore any difference in the rate of diffusion of the magnesium isotopes in the melt on the basis of our having measured these differences for calcium isotopes in similar liquids (Richter et al., 1999b) and found these to be negligibly small for present purposes. Figure 14d is a plot of the bulk $^{25}Mg/^{24}Mg$ after 50% of the magnesium has evaporated, as a function of the evaporation number. A useful parameterization for the effect of diffusion in the melt on the bulk isotopic fractionation of magnesium isotopes by evaporation is given by

$$\delta^{25}Mg_{bulk} \approx \delta^{25}Mg_{(Ev=0)}\, e^{-0.09Ev} \tag{24}$$

where $\delta^{25}Mg_{bulk} = 1000\,[(^{25}Mg/^{24}Mg)_{bulk}/(^{25}Mg/^{24}Mg)_0 - 1]$, $(^{25}Mg/^{24}Mg)_0$ is the unfractionated isotopic composition, and $\delta^{25}Mg_{(Ev=0)}$ is the fractionation calculated by the Rayleigh equation (Eqn. 5). Wang et al. (1999) calculated the effect of diffusion on the isotopic fractionation during evaporation from a diffusion-limited, finite-thickness slab rather than a sphere, and found the effect to be similar to what we report here. Their figure A3 shows decreasing isotopic fractionation as a function of a parameter W, the nondimensional velocity of the evaporating surface. W is also the ratio of the diffusive time scale to the evaporation time scale of a finite thickness slab, and thus it is the Cartesian coordinate equivalent of our nondimensional parameter E_v. Nagahara and Ozawa (2000) derive model equations for the isotopic fractionation of a condensed phase during congruent evaporation and measure the importance of diffusion in the melt in terms of an evaporation Peclet number (P_e), which is also closely related to the evaporation number used here ($P_e \equiv V_j J_{j,0} r_0/D_{j,0} = (V_j C_{j,0}/3)E_{vj}$ when $j = 1$ for congruent melting). For cases of incongruent evaporation, one could specify separate Peclet numbers for each of the evaporating components, but we prefer to use evaporation numbers because they seem to us a more direct measure of how diffusion affects individual components.

9. CONSTRAINTS ON THE THERMAL HISTORY OF TYPE B CAIS

As shown in Figure 1, Type B CAIs are often enriched in the heavy isotopes of silicon and magnesium relative to the terrestrial isotopic ratio of these elements. For magnesium isotopes, fractionations of 1 to 5‰ per atomic mass number are quite common. The purpose of this section is to translate these measured isotopic fractionations of the Type B CAIs into constraints on their thermal history by determining the conditions of temperature and hydrogen pressure required to effect the observed range of fractionations. We make use of the

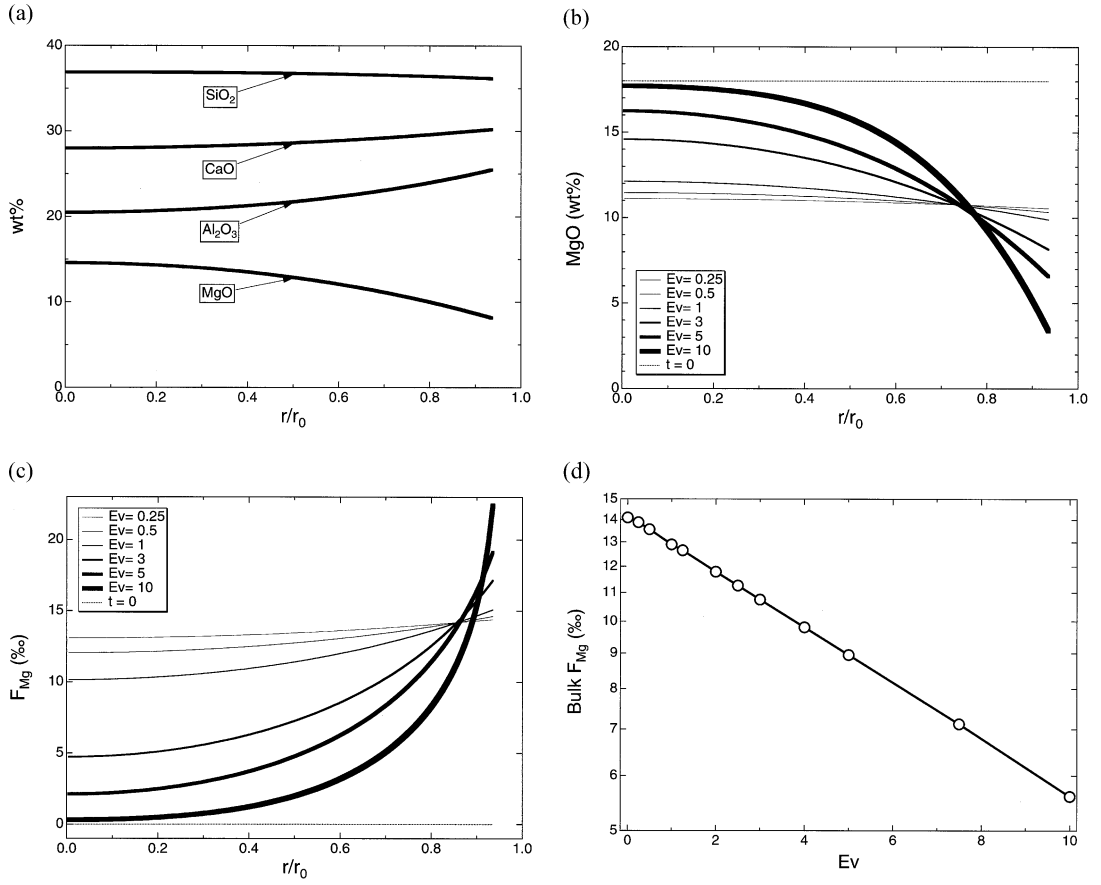

Fig. 14. (a) Concentration as a function of fractional radius in a molten sphere at a time such that 50% of the initial Mg has evaporated. Calculations are based on Eqn. 23 subject to Eqn. 23a and 23b with $E_{vMg} = 3.0$, $E_{vSi} = 0.7$, $E_{vCa} = E_{vAl} = 0$, $V_{MgO} = 0.15$, $V_{SiO_2} = 0.5$, $D_{MgO} = 1.0$, $D_{CaO} = 2.0$, $D_{Al_2O_3} = D_{SiO_2} = 0.5$. The profiles end at $r/r_0 = 0.95$, indicating that the radius has decreased by 5% due to evaporation of magnesium and silicon oxides (see text for details). (b) Concentration gradients of weight percentage of MgO as a function of fractional radius for different choices of the evaporation number E_v, all at a time such that 50% of the initial Mg has evaporated. $E_{vMg} = E_v$, $E_{vSi} = 0.25\ E_v$; all other quantities as in Figure 14a. The dotted curve at 18 wt% MgO is the initial condition. (c) Calculated profiles of $^{25}Mg/^{24}Mg$ (‰) relative to the starting composition corresponding to the concentration profiles shown in Figure 14b. (d) Bulk $^{25}Mg/^{24}Mg$ (‰) relative to the starting composition vs. magnesium evaporation number calculated from the concentration and isotopic profiles shown in Figures 14b,c.

parameterizations developed in section 7 because of their ease of implementation and the clarity with which they identify the various key factors such as temperature, hydrogen pressure, and sample size that affect the outcome.

We can illustrate the relationship between isotope fractionation and thermal history by calculating the linear cooling rate, starting from 1400°C, that produces 1 or 5‰ amu^{-1} fractionation of magnesium isotopes. Figure 15 shows the result based on Eqn. 17 applied to ^{24}Mg and ^{25}Mg. Several distinct regimes are evident. For hydrogen pressures up to $\sim 10^{-2}$ bar the rate of evaporation increases with pressure and therefore the cooling rate must also increase to maintain a fixed degree of isotopic fractionation. Once hydrogen pressures exceed $\sim 10^{-2}$ bar, recondensation becomes increasingly important, and slower cooling rates are required for a particular amount of isotope fractionation. There are two reasons for this. First, there is the decrease in the net evaporation rate due to recondensation as shown in Figure 12. Second, there is less isotopic fractionation associated with evaporation at the higher pressures, as can be seen from the effect of pressure on the effective isotopic fractionation factor (Fig. 13).

Figure 15 is illustrative of specific thermal histories (i.e., linear cooling from an instantaneous peak temperature of 1400°C) that are consistent with specific degrees of magnesium isotope fractionation. The general constraint on the thermal history is in the form of an integral, which is easily derived in the simplified case where we ignore the small change in radius associated with evaporation of a few tens of weight percent of SiO_2 and MgO. For a sphere of fixed radius a, the conservation equation is simply

$$\frac{d(VC_i)}{dt} = -J_i A, \tag{25}$$

where V is the volume, C_i is molar density, J_i is the evaporation flux, and A is the surface area. For fixed radius a, Eqn. 25 has the solution

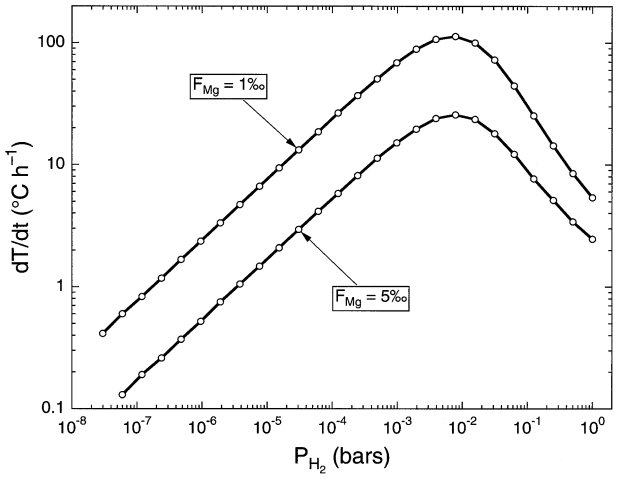

Fig. 15. Calculated curves show the linear cooling rate starting from 1400°C required for a molten 0.5-cm-radius Type B CAI sphere to fractionate magnesium isotopes by evaporation by 1 or 5‰ amu^{-1} for a broad range of hydrogen pressures. Calculation uses Eqn. 17 with a reference evaporation rate $J_{Mg}(T_0,P_0) = 3 \times 10^{-8}$ mol cm^{-2} s at T_0 = 1500°C and $P_0 = 1.87 \times 10^{-4}$ bar hydrogen, an activation energy of 300 kJ mol^{-1}, and an evaporation coefficient of 0.033. The temperature and pressure dependence of the diffusivity D of the evaporating species in the surrounding gas was calculated by Eqn. 16.

$$\frac{C_j(t)}{C_i(0)} = 1 - \frac{3}{aC_i(0)}\int_0^t J_i\,dt, \qquad (26)$$

where $C_i(0)$ is the initial molar density. For a given fractionation factor α' (from Eqn. 22) we can use Eqn. 5 to relate the fraction of a species remaining in the residue to the isotopic R/R_0 and write Eqn. 26 as

$$\int_0^t J_i\,dt = \frac{aC_i(0)}{3}\left(1 - 10^{\frac{\log(R/R_0)}{\alpha'-1}}\right). \qquad (27)$$

Eqn. 27 is, in effect, an integral constraint on the thermal evolution T(t) associated with a particular degree of isotopic fractionation R/R_0: T(t) must be such that the associated evolution of the evaporation flux J_i (t) satisfies Eqn. 27. While the linear cooling used to construct Figure 15 is only one of an infinite number of possible thermal histories satisfying Eqn. 27, it does serve to illustrate the characteristic cooling time of smoothly varying thermal histories that start from a peak temperature of ~1400°C.

We have not yet considered whether we can ignore, or should include, at least in a parameterized sense (e.g., Eqn. 24), the effect of diffusion in the melt when discussing the thermal evolution of typical Type B CAIs. Whether or not diffusion plays an important role depends on the evaporation number $E_{v,j}$ ($= 3J_{j,0}r_0/C_{j,0}D_{j,0}$) being large or small compared with one. We can use r_0 = 0.5 cm as a typical radius of a Type B CAI. For the evaporation of magnesium at T = 1400°C and $P_{H_2} = 2 \times 10^{-4}$ bar, we have $J_{Mg,0} \approx 1 \times 10^{-8}$ mol cm^{-2} s^{-1} (based on the average magnesium evaporation rate of the BCAI experiments adjusted to T = 1400°C) and a molar density $C_{j,0} \approx 0.01$ (mol/cm^3). $D_{Mg,0} \approx 1 \times 10^{-6}$ cm^2 s^{-1} is a reasonable estimate of the effective chemical diffusivity of Mg in a Type B CAI-like liquid at 1400°C. This results in an estimate of $E_{v,Mg} \approx 1$, which suggests that diffusion is not terribly important in connection with evaporation of the Type B CAIs in 2×10^{-4} bar hydrogen. The value we used for $D_{Mg,0}$ was arrived at by first estimating the mobilities of all the oxide components in a Type B CAI liquid on the basis of mobility–composition relationships such as those given in Liang et al. (1996). We estimate that the mobility of magnesium at T = 1400°C is 1.3×10^{-6} cm^2 s^{-1}, in good agreement with extrapolations of reported values given by Sheng et al. (1992) and by LaTourrette et al. (1996). We then used the estimated mobilities in a Cooper nonideal molecular model (see Liang et al., 1997) to construct a chemical diffusion matrix for the Type B CAI liquid. The final step was to use the diffusion matrix to calculate effective binary diffusion coefficients for the oxide components along the compositional direction associated with evaporation. The binary diffusion coefficients calculated for a Type B CAI composition at T = 1400°C are $D_{Ca} = 2.0 \times 10^{-6}$ cm^2 s^{-1}, $D_{Mg} = 1.0 \times 10^{-6}$ cm^2 s^{-1}, and $D_{Si} = 0.5 \times 10^{-6}$ cm^2 s^{-1}. These are the effective binary diffusion coefficients used to specify the parameters used in connection with Figure 14.

Whether or not diffusion in the liquid is important in terms of the bulk isotopic fractionation of a typical Type B CAI will depend to a large degree on the hydrogen pressure. Temperature is far less important in that the activation energy for diffusion is quite similar to that for evaporation into hydrogen (~300 kJ mol^{-1} K^{-1}). We estimated that $E_{v,Mg} \approx 1$ for $P_{H_2} = 2 \times 10^{-4}$ bar, in which case diffusive gradients in the melt are not large and the isotopic fractionation for a given amount of evaporative loss is reduced (relative to perfect Rayleigh fractionation) by only ~10% (see Eqn. 24). At lower hydrogen pressures the evaporation rate is lower, and thus finite diffusion has a correspondingly lesser effect on isotope fractionation. However, at hydrogen pressures of about $P_{H_2} = 10^{-2}$ bar, the net evaporation rate is significantly greater than that at $P_{H_2} = 2 \times 10^{-4}$ bar (Fig. 12), by about a factor of 10 , and thus for samples of comparable size, the evaporation number will also be greater by about a factor of 10 at the higher pressure. As shown in Figure 14d, the bulk isotopic fractionation is reduced by ~50% when the evaporation number is 10. The recurring theme is that in the specific context of constraints on the thermal history of Type B CAIs, the most important quantity is the hydrogen pressure. Taking diffusion in the liquid into account could, for large evaporation number, change the estimated cooling rate by a factor of about two. This should be compared with the effect of hydrogen pressure shown in Figure 15, where the cooling rate for a given degree of isotope fractionation differs by an order of magnitude or more depending on the hydrogen pressure ($P_{H_2} = 10^{-2}$ to 10^{-5} bar) that prevailed during the reheating event that melted the Type B CAIs.

We should note in closing this section that we have made no allowance for the effect of crystallization on melt composition. Eqn. 10 shows how crystallization enters the diffusion equation. In a subsequent article, we will consider the combined effects of evaporation, crystallization, and chemical diffusion. We do not expect that the results given here will be significantly affected, however the combined effects of evaporation, crystallization and diffusion in the melt may provide some

insight into why certain Type B inclusions, the B2s, have a relatively uniform spatial distribution of mineral phases whereas the B1s have melilite-dominated outer mantles.

10. SUMMARY AND DISCUSSION

We have shown, by experiment, the following.

(1) Evaporation of molten Type B CAI-like compositions in vacuum or in a hydrogen-dominated gas preferentially removes silicon and magnesium leaving behind a residue enriched in calcium and aluminum (see Table 1).

(2) The relative rates of evaporation of silicon and magnesium reflect the saturation vapor pressure of the gas species they produce (mainly SiO and Mg) and thus depend on composition. In general, compositions with greater than 35 wt% SiO_2 evaporate silicon more rapidly than magnesium, with the rates becoming comparable for SiO_2 contents of 35 wt% or less (see Fig. 2 and Hashimoto, 1983).

(3) The measured rates of silicon and magnesium evaporation are proportional to the calculated saturation vapor pressure of SiO and Mg with a proportionality constant (the evaporation coefficient) much less than one (Fig. 10).

(4) Evaporation residues of samples run in vacuum and in hydrogen are similarly enriched in the heavy isotopes of magnesium with a kinetic fractionation factor close to, but not exactly, the theoretically expected value (Figs. 5 and 9).

(5) The range of magnesium isotopic compositions of Type B CAIs (Fig. 1), if produced by evaporative loss of magnesium, requires magnesium losses from 0 to ~50% (Figs. 5 and 9).

We have used various theoretical relationships along with a thermodynamic representation of Type B CAI-like liquids to explain and parameterize the dependence of the evaporation rate and isotopic fractionation of silicon and magnesium as a function of composition, temperature, hydrogen pressure, and diffusion in the surrounding gas and in the melt. We then used the parameterizations to translate typical magnesium isotopic fractionations of the Type B CAIs into constraints on their thermal history. The overall conclusion is that the Type B CAIs, which on the basis of petrologic and textural evidence were reheated to ~1400°C (Stolper, 1982), must have cooled at rates of the order of degrees or tens of degrees per hour. We are not the first to suggest that the rates of cooling of the Type B CAIs were of the order of °C h^{-1}. Stolper and Paque (1986) made an excellent case that the cooling rates could not have been faster than ~50°C h^{-1} on the basis of the texture of the coarse-grained inclusions. Our main contribution is in connection with the lower bound on the cooling rate, where we have shown that cooling rates slower than 1 to 100°C h^{-1}, depending on the hydrogen pressure, would result in unacceptably large isotopic fractionation of silicon and magnesium. Allowable cooling rates are clearly not hundreds of degrees Celsius per second, as would be the case for radiative cooling in optically thin regions or degrees per thousands of years which would be characteristic of the thermal evolution of the protoplanetary disk as a whole.

Numerous suggestions have been made as to the process or processes responsible for melting chondrules and CAIs (see Boss, 1996, for a concise guide to chondrule formation models). These range from local (e.g., impact melting, nebular lightning) to large scale (e.g., high-temperature inner nebula). Gas drag and collisions associated with accretionary or nebular shocks are an often-cited possibility. However, there is no generally accepted model for melting chondrules and CAIs, in large part for lack of quantitative constraints with which to validate or reject specific models. Focusing on the cooling history, as we have done for the Type B CAIs, may well provide some important discrimination.

Local transient heating processes such as lightning or impact melting will be followed by such rapid cooling (100°C s^{-1}; see fig. 3 in Horányi and Robinson, 1996) that they do not appear to be a plausible mechanism to explain the thermal history of coarse-grained CAIs. Heating mechanisms associated with shock waves (Hood and Horányi, 1991, 1993; Wood, 1984) are probably the most often mentioned explanation for the high temperatures required by chondrule formation and thus could certainly also be considered in terms of melting the CAI precursors. However, the subsequent cooling would very likely have been determined by radiation into a moderate temperature (100 to 500 K) surrounding medium resulting in cooling rates of degrees per second (Ruzmaikina and Ip, 1996), which is still orders of magnitude faster than what the textures of Type B CAIs will allow. If the transient heating took place in a sufficiently optically thick region the cooling rates could have been much slower, but in general, it would seem that local heating events, by their very nature, will result in too rapid cooling to be a reasonable explanation for partially melting the coarse-grained CAIs.

A promising explanation for how CAIs were heated to ~1400°C and then cooled at rates of the order of 10°C h^{-1} is that they were entrained by aerodynamic drag into the magnetocentrifugally driven wind from our young sun (Shu et al., 1996, and references therein). The heating of the proto-CAIs (and their sorting by size) is accomplished when solid bodies moving toward the sun in the relatively cool disk are lifted along outward trajectories where they are exposed to much more direct sunlight. The size sorting depends on the size of the aerodynamic coupling constant, which in turn is inversely proportional to particle size. Small particles such that the coupling constant is large will escape from the evolving solar system; large particles decouple from the outflow and fall back onto the disk to be recycled (see also Liffman and Brown, 1995). Only a relatively narrow range of sizes will result in trajectories that can be regarded as candidates for having produced the CAIs and the time of flight along these is of the order of several tens of days (see fig. 2 in Shu et al., 1996). The high-temperature stage will be considerably shorter than this, and thus the temperature histories of particles along suitable trajectories could well be compatible with the constraint given by Eqn. 27.

Shu et al. (1996) end their article by saying that "the richest confrontation between theory and data, however, may still come from the chondritic meteorites." We hope our efforts reported here will be seen as a useful step in translating some of the chemical and isotopic data from the Type B CAIs into constraints more directly useful for the confrontation of theory and data.

Acknowledgments—We thank A. Tsuchiyama, G. R. Huss, U. Ott, and an anonymous reviewer for their detailed and constructive reviews. The work reported here was supported by NASA grants NAG5-9378

(F.M.R.), NAG5-9510 (A.M.D.), NAG5-4476 (D.S.E.), and by Japan Ministry of Education via grant Kiban-C, 11640436 (A.H.).

Associate editor: U. Ott

REFERENCES

Allègre C. J., Manhès G., and Göpel C. (1995) The age of the Earth. *Geochim. Cosmochim. Acta* **59,** 1445–1456.

Balat M., Flamant G., Male G., and Pichelin G. (1992) Active to passive transition in the oxidation of silicon-carbide at high-temperature and low pressure in molecular and atomic oxygen. *J. Mater. Sci.* **27,** 697–703.

Beckett J. R. (1986) The origin of calcium-, aluminum-rich inclusions from carbonaceous chondrites: An experimental study. Ph.D. thesis. University of Chicago.

Beckett J. R., Spivack A. J., Hutcheon I. D., Wasserburg G. J., and Stolper E. M. (1990) Crystal chemical effects on the partitioning of trace elements between mineral and melt: An experimental study of melilite with applications to refractory inclusions from carbonaceous chondrites. *Geochim. Cosmochim. Acta* **54,** 1755–1774.

Berman R. G. (1983) A thermodynamic model for multicomponent melts, with application to the system CaO-MgO-Al_2O_3-SiO_2. Ph.D. thesis. University of British Columbia.

Boss A. P. (1996) A concise guide to chondrule formation models. In *Chondrules and the Protoplanetary Disk* (eds. R. H. Hewins, R. H. Jones, and E. R. D. Scott), pp. 257–263. Cambridge University Press.

Boss A. P. (1998) Temperature in protoplanetary disks. *Annu. Rev. Earth Planet. Sci.* **26,** 53–80.

Clayton R. N., Hinton R. W., and Davis A. M. (1988) Isotopic variations in the rock-forming elements in meteorites. *Phil. Trans. R. Soc. Lond. A* **325,** 483–501.

Davis A. M., Hashimoto A., Clayton R. N., and Mayeda T. K. (1990) Isotope mass fractionation during evaporation of Mg_2SiO_4. *Nature* **347,** 655–658.

Davis A. M. and MacPherson G. J. (1996) Thermal processing in the solar nebula: Constraints from refractory inclusions. In *Chondrules and the Protoplanetary Disk* (eds. R. H. Hewins, R. H. Jones, and E. R. D. Scott), pp. 71–76. Cambridge University Press.

Davis A. M., Richter F. M., Simon S. B., and Grossman L. (1996) The effect of cooling rate on melilite/liquid partition coefficients for Y and REE in type B CAI melts. *Lunar Planet. Sci.* **27,** 291–292.

Dowty E. and Clark J. R. (1973) Crystal structure refinement and optical properties of a Ti^{+3} fassaite from the Allende meteorite. *Am. Mineral.* **58,** 230–242.

Geankoplis C. J. (1962) *Mass Transport Phenomena.* Holt, Rinehart and Winston.

Grossman L. (1972) Condensation in the primitive solar nebula. *Geochim. Cosmochim. Acta* **36,** 597–619.

Grossman L., Ebel D. S., Simon S. B., Davis A. M., Richter F. M., and Parsad N. M. (2000) Major element chemical and isotopic compositions of refractory inclusions in C3 chondrites: The separate roles of condensation and evaporation. *Geochim. Cosmochim. Acta* **64,** 2879–2894.

Hashimoto A. (1983) Evaporation metamorphism in the early solar nebula—Evaporation experiments on the melt FeO-MgO-SiO_2-CaO-Al_2O_3 and chemical fractionations of primitive materials. *Geochem. J.* **17,** 111–145.

Hashimoto A. (1990) Evaporation kinetics of forsterite and implications for the early solar nebula. *Nature* **347,** 53–55.

Hashimoto A. (1998) Absolute reaction rates of hydrogen with condensed phases in the nebula. *Meteor. Planet. Sci.* **33,** A65.

Hashimoto A. (1999) Chemical and isotopic fractionations in the primordial nebula. *Planet. People* **4,** 266–282.

Hirth J. P. and Pound G. M. (1963) *Condensation and Evaporation.* Macmillan.

Hood L. L. and Horányi M. (1991) Gas dynamic heating of chondrule precursor grains in the solar nebula. *Icarus* **93,** 259–269.

Hood L. L. and Horányi M. (1993) The nebular shock wave model for chondrule formation: One-dimensional calculations. *Icarus* **106,** 179–189.

Horányi M. and Robertson S. (1996) Chondrule formation by lightning discharges: Status of theory and experiments. In *Chondrules and the Protoplanetary Disk* (eds. R. H. Hewins, R. H. Jones, and E. R. D. Scott), pp. 303–310. Cambridge University Press.

Humayun M. and Cassen P. (2000) Processes determining the volatile abundances of the meteorites and terrestrial planets. In *Origin of the Earth and Moon* (eds. R. M. Canup and K. Righter), pp. 3–23. University of Arizona Press.

Kuroda D. and Hashimoto A. (2000a) The reaction of forsterite with hydrogen—Its apparent and real temperature dependences. *Antarctic Meteor.* **25,**64–66.

Kuroda D. and Hashimoto A. (2002) The reaction of forsterite with hydrogen—Its apparent and real temperature dependences. *Antarctic Meteor.*,in press.

Kuroda D. and Hashimoto A. (2000b) The reaction of forsterite with hydrogen under nebular P-T conditions. *Proc. ISAS Symp.* **33,** 80–83.

LaTourrette L., Wasserburg G. J., and Fahey A. J. (1996) Self diffusion of Mg, Ca, Ba, Nd, Yb, Ti, Zr, and U in haplobasaltic melt. *Geochim. Cosmochim. Acta* **60,** 1329–1340.

Liang Y., Richter F. M., Davis A. M., and Watson E. B. (1996) Diffusion in silicate melts: I. Self diffusion in CaO-Al_2O_3-SiO_2 at 1500°C and 1 GPa. *Geochim. Cosmochim. Acta* **60,** 4353–4367.

Liang Y., Richter F. M., and Chamberlin L. (1997) Diffusion in silicate melts: III. Empirical models for multicomponent diffusion. *Geochim. Cosmochim. Acta* **61,** 5295–5312.

Liffman K. and Brown M. (1995) The motion and size sorting of particles ejected from a protostellar accretion disk. *Icarus* **116,** 275–290.

MacPherson G. J., Paque J. M., Stolper E., and Grossman L. (1984) The origin and significance of reverse zoning in melilite from Allende type B inclusions. *J. Geol.* **92,** 289–305.

MacPherson G. J., Davis A. M., and Zinner E. K. (1995) The distribution of aluminum-26 in the early Solar System—A reappraisal. *Meteoritics* **30,** 365–386.

Mendybaev R. A., Beckett J. R., Stolper E., and Grossman L. (1998) Measurement of oxygen fugacities under reducing conditions: Non-Nernstian behavior of Y_2O_3-doped zirconia oxygen sensors. *Geochim. Cosmochim. Acta* **62,** 3131–3139.

Nagahara H. and Ozawa K. (1996) Evaporation of forsterite in H_2 gas. *Geochim. Cosmochim. Acta* **60,** 1445–1459.

Nagahara H. and Ozawa K. (2000) Isotopic fractionation as a probe of heating processes in the solar nebula. *Chem. Geol.* **169,** 45–68.

Parsad N., Richter F. M., Davis A. M., and Hashimoto A. (2000) Elemental and isotopic fractionation of CAI liquids at T = 1773K and $P_{H_2} = 1.9 \times 10^{-4}$ bar [abstract 1956]. In *Lunar and Planetary Science* **31**. Lunar and Planetary Institute (CD-ROM).

Richter F. M., Parsad N. M., Davis A. M., and Hashimoto A. (1999a) CAI cosmobarometry [abstract 1989]. In *Lunar and Planetary Science* **30**. Lunar and Planetary Institute (CD-ROM).

Richter F. M., Liang Y., and Davis A. M. (1999b) Isotope fractionation by diffusion in molten oxides. *Geochim. Cosmochim. Acta* **63,** 2853–2861.

Russell S. S., Davis A. M., MacPherson G. J., Guan Y., and Huss G. R. (2000) Refractory inclusions from the ungrouped carbonaceous chondrites MacAlpine Hills 87300 and 88107. *Meteor. Planet. Sci.* **35,** 1051–1066.

Ruzmaikina T. and Ip W. H. (1996) Chondrule formation in the accretional shock. In *Chondrules and the Protoplanetary Disk* (eds. R. H. Hewins, R. H. Jones, and E. R. D. Scott), pp. 277–284. Cambridge University Press.

Sheng Y. J., Wasserburg G. J., and Hutcheon I. D. (1992) Self-diffusion of magnesium in spinel and in equilibrium melts: Constraints on flash heating of silicates. *Geochim. Cosmochim. Acta* **56,** 2535–2546.

Shu F. H., Shang H., and Lee T. (1996) Toward an astrophysical theory of chondrites. *Science* **271,** 1545–1552.

Simon S. B., Davis A. M., Richter F. M., and Grossman L. (1996) Experimental investigation of the effect of cooling rate on melilite/liquid distribution coefficients for Sr, Ba, and Ti in type B refractory inclusion melts. *Lunar Planet. Sci.* **27,** 1201–1202.

Stolper E. (1982) Crystallization sequences of calcium-aluminum–rich

inclusions from Allende: An experimental study. *Geochim. Cosmochim. Acta* **46,** 2159–2180.

Stolper E. and Paque J. M. (1986) Crystallization sequences of calcium-aluminum–rich inclusions from Allende: The effects of cooling rate and maximum temperature. *Geochim. Cosmochim. Acta* **50,** 1785–1806.

Tsuchiyama A., Takahashi T., and Tachibana S. (1998) Evaporation rates of forsterite in the system Mg_2SiO_4-H_2. *Mineral. J.* **20,** 113–126.

Tsuchiyama A., Tachibana S., and Takahashi T. (1999) Evaporation of forsterite in the primordial solar nebula; rates and accompanied isotopic fractionation. *Geochim. Cosmochim. Acta* **63,** 2451–2466.

Wang J., Davis A. M., Clayton R. N., and Hashimoto A. (1999) Evaporation of single crystal forsterite: Evaporation kinetics, magnesium isotope fractionation, and implications of mass-dependent isotopic fractionation of a diffusion-controlled reservoir. *Geochim. Cosmochim. Acta* **63,** 953–966.

Wang J., Davis A. M., Clayton R. N., Mayeda T. K., and Hashimoto A. (2001) Chemical and isotopic fractionation during the evaporation of the FeO-MgO-SiO_2-CaO-Al_2O_3-TiO_2-REE melt system. *Geochim. Cosmochim. Acta* **65,** 479–494.

Williams R. J. and Mullins O. (1976) *A System Using Solid Ceramic Oxygen Electrolyte Cells to Measure Oxygen Fugacities in Gas-Mixing Systems. NASA Technical Memorandum 58167*. NASA.

Wood J. A. (1984) On the formation of meteoritic chondrules by aerodynamic drag heating in the solar nebula. *Earth Planet. Sci. Lett.* **70,** 11–26.